

AD-A261 646

2

PL-TR-92-2215



**DATA ANALYSIS SUPPORT FOR THE SHUTTLE
POTENTIAL AND RETURN ELECTRON EXPERIMENT
(SPREE) ON THE TETHERED SATELLITE
SYSTEM 1 (TSS-1) FLIGHT**

**M. J. Mandell
V. A. Davis
I. Katz
G. A. Jongeward**

**Maxwell Laboratories, Inc.
S-Cubed Division
P. O. Box 1620
La Jolla, California 92038-1620**



29 June 1992

Scientific Report No. 2

93-02319



Approved for public release; distribution unlimited



**PHILLIPS LABORATORY
Directorate of Geophysics
AIR FORCE SYSTEMS COMMAND
HANSCOM AIR FORCE BASE, MA 01731-5000**

"This technical report has been reviewed and is approved for publication."



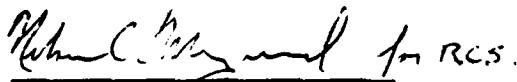
(Signature)

MARILYN R. OBERHARDT
Contract Manager



(Signature)

E.G. MULLEN
Branch Chief



(Signature)

RITA C. SAGALYN
Division Director

This report has been reviewed by the ESD Public Affairs Office (PA) and is releasable to the National Technical Information Service (NTIS).

Qualified requestors may obtain additional copies from the Defense Technical Information Center. All others should apply directly to the National Technical Information Service.

If your address has changed, or if you wish to be removed from the mailing list, or if the addressee is no longer employed by your organization, please notify PL/TSI, Hanscom AFB, MA 01731. This will assist us in maintaining a current mailing list.

Do not return copies of this report unless contractual obligations or notices on a specific document require that it be returned.

REPORT DOCUMENTATION PAGE			Form Approved OMB No. 0704-0188	
Public reporting burden for this collection of information is estimated to average 1 hour per response, including the time for reviewing instructions, searching existing data sources, gathering and maintaining the data needed, and completing and reviewing the collection of information. Send comments regarding this burden estimate or any other aspect of this collection of information, including suggestions for reducing this burden, to Washington Headquarters Services, Directorate for Information Operations and Reports, 1215 Jefferson Davis Highway, Suite 1204, Arlington VA 22202-4302, and to the Office of Management and Budget, Paperwork Reduction Project (0704-0188), Washington, DC 20503				
1. AGENCY USE ONLY (Leave blank)		2. REPORT DATE June 29, 1992	3. REPORT TYPE AND DATES COVERED Scientific Report No. 2	
4. TITLE AND SUBTITLE "Data Analysis Support for the Shuttle Potential and Return Electron Experiment (SPREE) on the Tethered Satellite System 1 (TSS-1) Flight"			5. FUNDING NUMBERS F19628-90-C-0133 PE 63410F PR 2822 TA01 WUAK	
6. AUTHOR(S) M. J. Mandell I. Katz V. A. Davis G. A. Jongeward				
7. PERFORMING ORGANIZATION NAME(S) AND ADDRESS(ES) Maxwell Laboratories, Inc. S-Cubed Division P. O. Box 1620 La Jolla, CA 92038-1620			8. PERFORMING ORGANIZATION REPORT NUMBER SSS-DTR-92-13437	
9. SPONSORING/MONITORING AGENCY NAME(S) AND ADDRESS(ES) Phillips Laboratory Hanscom Air Force Base, MA 01731-5000 Contract Manager: Capt. M. Oberhardt/GPSP			10. SPONSORING/MONITORING AGENCY REPORT NUMBER PL-TR-92-2215	
11. SUPPLEMENTARY NOTES				
12a. DISTRIBUTION/AVAILABILITY STATEMENT Approved for public release; distribution unlimited			12b. DISTRIBUTION CODE	
13. ABSTRACT (Maximum 200 words) This report describes the second year of a scientific study of the interactions between the first flight of the Tethered Satellite System (TSS-1) and the ionosphere to increase understanding of the structure and current characteristics of high-voltage sheaths in the ionosphere. The investigations described here include an examination of electron collection and presheath structure by a positively biased, conducting sphere in the ionosphere moving at orbital velocity, including the effects of the earth's magnetic field and the current collection capabilities of the TSS-1 subsatellite considering the revised conductivity measurements.				
14. SUBJECT TERMS tether, TSS-1, shuttle, current collection, SPREE			15. NUMBER OF PAGES 94	
			16. PRICE CODE	
17. SECURITY CLASSIFICATION OF REPORT Unclassified	18. SECURITY CLASSIFICATION OF THIS PAGE Unclassified	19. SECURITY CLASSIFICATION OF ABSTRACT Unclassified	20. LIMITATION OF ABSTRACT SAR	

TABLE OF CONTENTS

Section	Page
1. Introduction	1
2. Positive Orbital Probe Collection	3
2.1 Introduction	3
2.2 Estimate of Ion Density at the Stagnation Surface	4
2.3 Particle-Tracking Waterbag Code for Ion Densities	6
2.4 Estimate of Stagnation Surface and Current for a High-Voltage Sphere	10
2.5 A Model for a Resistive Presheath	13
2.5.1 The Current Definition Equation	13
2.5.2 The Equation for the Potential	14
2.5.3 The Heat Flux Definition Equation	14
2.5.4 The Equation for the Temperature	14
2.5.5 Scaling	14
2.5.6 Finite Element Solution	15
2.5.7 Defining a Problem	15
2.5.8 Example 1: A Spherical Stagnation Surface	16
2.5.9 Example 2: A Realistic Stagnation Surface	18
3. Consistent Solution for Current to Orbital Probe	23
4. Ion Stagnation in a Repulsive Coulomb Potential	29
4.1 Introduction	29
4.2 Nomenclature	29
4.3 Stagnation Surface at Zero Temperature	30
4.4 Density Along the Symmetry Axis	33
4.5 Density at an Arbitrary Point	36
5. Sheath Structure about a Spherical Probe	41
5.1 Introduction	41
5.2 Chaotic Orbits and Orbit-Limited Density	41

TABLE OF CONTENTS (continued)

Section	Page
5.3 Transformation to Dimensionless Units.....	43
5.4 Computational Results.....	45
5.5 Conclusions.....	52
6. Three-Dimensional Magnetic Sheath Calculations.....	53
7. Analysis of High Resistance Paint on the TSS-1 Subsatellite Sheath	59
7.1 Analysis and Calculations of the Present Subsatellite Configuration.....	59
7.1.1 Analysis of the Sheath Potentials Surrounding the Belly Band.....	60
7.1.2 Analysis of ITO Coating on the Satellite.....	63
7.1.3 Electron Collection by Surface Snapover.....	64
7.2 Conclusions.....	67
References.....	69
Attachment 1.....	71

Accession For	
NTIS GRA&I	<input checked="" type="checkbox"/>
DTIC TAB	<input type="checkbox"/>
Unannounced	<input type="checkbox"/>
Justification.....	
By.....	
Distribution/	
Availability Codes	
Dist.	Avail and/or Special
A-1	

DTIC QUALITY INSPECTED 3

LIST OF FIGURES

Figure	Page
1. Theoretical estimate of relative density at the stagnation surface vs. angle-corrected Mach number, $V \cos \psi / (2e\theta / m)^{1/2}$	5
2. Particle trajectories for ram ions incident on a spherical equipotential at the stagnation energy:(a) trajectories up to closest approach to sphere; (b) trajectories beyond closest approach to sphere. The potential field is Laplacian.....	7
3. Trajectory divergence in a Laplacian potential. The ordinate is the distance from the symmetry axis divided by the radius of the spherical equipotential at the stagnation energy. The density is reduced by the square of this factor.	8
4. Calculated density contours for ram ions incident on a spherical Laplacian potential. The contour increment is 0.2, with the outermost relative density being 1.2.....	9
5. Calculated potential contours for a 5000 volt, 1 m radius sphere in a 5 eV ram plasma. (See text for other computational parameters.) (The negative potential island at center-right is an artifact of the gridding.)	12
6. Axisymmetric finite element grid used for spherical stagnation surface example. The grid is composed of biquadratic elements. Symbols "1" and "2" label the outer (ambient) and inner (stagnation) boundaries, respectively.....	16
7. Calculated equipotential contours for the spherical stagnation surface example. The contour increment is 0.5 volts.....	17
8. Calculated equithermal contours for the spherical stagnation surface example. The contour increment is 0.05 eV. A broad temperature maximum of about 1 eV appears outside the stagnation surface.	17

LIST OF FIGURES (continued)

Figure	Page
9. Axisymmetric finite-element grid used for studying the presheath outside a realistic stagnation surface. The stagnation surface (marked "2") is based on the parameters quoted in the previous section. The grid extends 4 m wakeward, 8 m ramward, and 8 m outward, from the center of a 1 m radius sphere (not show) at 5 kV.	19
10. Assumed ion density contours (computed as described in the text) outside the stagnation surface.....	19
11. Calculated equipotential contours in the resistive presheath.	20
12. Calculated equithermal contours in the resistive presheath.	20
13. Particle trajectories for ram ions incident on the resistive presheath potentials shown in Figure 11: (a) trajectories up to closest approach to sphere; (b) trajectories beyond closest approach to sphere.	21
14. Relative ion densities calculated from the trajectories shown in Figure 13.	22
15. Trajectory divergence for the trajectories of Figure 13, as a function of distance from the symmetry axis. (Compare with Figure 3.)	22
16. Potentials about the moving probe calculated using the inner sheath model (a) logarithmically spaced contours; (b) uniformly spaced contours.....	25
17. Potentials (a) and temperatures (b) in the presheath calculated using the resistive presheath model.	26
18. Ion trajectories in the potentials of Figure 17.....	27
19(a). Ram ion trajectories in a coulomb potential, showing trajectory crossings.	31

LIST OF FIGURES (continued)

Figure	Page
19(b). Incoming portion of the trajectories of Figure 19(a).....	32
19(c). Outgoing portion of the trajectories of Figure 19(a).....	32
20. The function $w(z)$, giving trajectory spread along the symmetry axis. Lower branch is for incoming trajectories, and upper branch for outgoing trajectories.....	34
21. Density along the symmetry axis for Mach 7 (broad curve) and Mach ∞ (sharply peaked curve).....	35
22(a). Ion densities for Mach 1. The boundaries of the figure are $0 < r < 10a_0$ and $-10 < z/a_0 < 3$, with an excluded sphere of radius $0.5a_0$	37
22(b). Ion densities for Mach 3.....	38
22(c). Ion densities for Mach 7.....	38
22(d). Ion densities for Mach 10.	39
22(e). Ion densities for Mach 30.	39
22(f). Ion densities for Mach 100.....	40
23. Computational grid of biquadratic elements, representing the region outside a sphere and within a cylinder of radius-20 sphere radii and height-40 sphere radii. Azimuthal and mirror symmetries are assumed.....	46
24. Electron density ratio contours calculated for potentials obeying Laplace's equation.....	47
25. Potential contours (a) and electron ratio contours (b) for density $Q_0 = 0.12$	48

LIST OF FIGURES (continued)

Figure	Page
26. Potential contours (a) and electron density ratio contours (b) for density $Q_0 = 0.28$	49
27. Potential contours (a) and electron density ratio contours (b) for density $Q_0 = 0.42$	50
28. Potential contours (a) and electron density ratio contours (b) for density $Q_0 = 0.69$	51
29. Radii of magnetic field lines contributing to densities at various radii on the symmetry plane. Outermost envelope, $Q_0 = 0.12$; second envelope, $Q_0 = 0.28$; third envelope, $Q_0 = 0.42$; innermost envelope, $Q_0 = 0.69$	52
30. Plasma wake densities for an uncharged, 0.8 m radius sphere.	53
31. Electrostatic potentials calculated with the sphere at 1000 volts and the ion densities of Figure 30.	54
32. Ion densities calculated using the ion stagnation surface as a shadowing surface.	55
33. Electrostatic potentials calculated using ion densities similar to Figure 32, and a space charge formulation allowing the wake to be electron rich.....	56
34. Tracked electron densities in the sheath region, with a magnetic field of 0.4 gauss in the y direction (a) X-Y plane; (b) X-Z plane; (c) Y-Z plane.	57
35. Electrostatic potentials calculated using the tracked electron densities in the sheath region (a) X-Y plane; (b) X-Z plane; (c) Y-Z plane.	58

1. INTRODUCTION

This interim report covers the period June 24, 1991 to June 28, 1992, and describes the scientific progress on Contract F19628-90-0133 entitled "Data Analysis Support for the SPREE Instruments on the TSS-1 Shuttle Flight." The objective of this contract is a scientific study of the interactions between the first flight of the Tethered Satellite System (TSS-1) and the ionosphere to increase understanding of the structure and current characteristics of high-voltage sheaths in the ionosphere.

During the second year of this contract, we examined electron collection and presheath structure by a positively biased, conducting sphere in the ionosphere moving at orbital velocity, including the effects of the earth's magnetic field. We examined the current collection capabilities of the TSS-1 subsatellite considering the revised conductivity measurements. And we provided support for the TSS-1 program.

During the second year of this contract, we prepared a paper describing some of the work during the first year for the AIAA 30th Aerospace Sciences Meeting in Reno Nevada in January 1992. This paper is in Attachment 1 to this report.

The technical staff who contributed to the research described in this report are I. Katz, M. J. Mandell, and G. A. Jongeward.

2. POSITIVE ORBITAL PROBE COLLECTION

2.1 Introduction

This attachment describes a collection of algorithms leading toward a theory of sheath structure and electron collection for a large orbital probe at high-positive potential. Presently, algorithms do not take into account magnetic field effects, except insofar as such effects may cause scattering and thermalization of electrons. Magnetic effects in the sheath will be included at a later date.

The theories assume that turbulent and scattering effects take place on a scale comparable to a debye length, so that the large-scale structure has a quiescent steady state. The main feature of the problem is a "stagnation surface" at which the ion density peaks. Within (or behind) the stagnation surface is a high-voltage region, in which the ion density drops extremely rapidly, and space charge consists of electrons in transit from the stagnation surface to the probe. Outside the stagnation surface (in the "presheath region") the plasma is assumed to be a "quasi-neutral" resistive medium, with transport of charge and energy by electrons. The challenge is to calculate the shape, density, and temperature of the stagnation surface, consistent with the physics in the presheath region, in the high-voltage region, and on the stagnation surface itself.

We have developed analytic and numerical methods to attack this problem, and have had some success at coupling these together. These include:

1. An analytic estimate for the local density at the stagnation surface, as a function of Mach number and angle of attack;
2. A particle-tracking "waterbag" computer code which, for known or assumed potentials, can estimate the shape of the stagnation surface, the density in the presheath region, and the density correction at the stagnation surface due to finite geometry (trajectory spreading) effects;

3. An axisymmetric code (specialized to a sphere) to estimate the shape of the stagnation surface and the total current transported from the stagnation surface to the probe, approximately consistent with the potential and space-charge structure in the high-voltage region.
4. An axisymmetric code (not necessarily specialized to a sphere) to estimate the potential and temperature fields in the presheath region for specified density and resistivity.

For various reasons (mostly numerical but occasionally physical), it is difficult to couple all of these techniques together to achieve a fully self-consistent solution. In particular, the presheath code probably requires a nonlinear (i.e., current dependent) resistivity in order to reasonably match a sensible current boundary condition at the stagnation surface. Nonetheless, the results here provide some insight into the density and potential structure for this problem, allow some estimate to be made for the current collection by the probe, and allow some evaluation of the assumptions in the theories.

2.2 Estimate of Ion Density at the Stagnation Surface

Suppose the stagnation surface to be locally a plane equipotential whose normal is at angle ψ to the flow direction. We can ignore ion motion along the surface. In the direction normal to the surface, the ion velocity distribution is a gaussian centered about $V \cos \psi$ (where V is the spacecraft velocity), so that the stagnation surface potential is $mV^2 \cos^2 \psi / 2e$.

Let
$$\beta^2 = \frac{m}{2e\theta}$$
 ,

and omit the $\cos \psi$ factor (which always appears with V). The density at the stagnation surface is then given by

$$\rho_s = \left(\frac{2n_0\beta}{\sqrt{\pi}} \right) \int_V^\infty \frac{v}{\sqrt{v^2 - V^2}} e^{-\beta^2(v-V)^2} dv$$

$$= n_0 \sqrt{\frac{2\beta V}{\pi}} \int_0^\infty \frac{(1+u/\beta V)}{\sqrt{u(1+u/2\beta V)}} e^{-u^2} du$$

(Note that βV is the Mach number.)

For $\beta V \gg 1$, we get

$$\frac{\rho_s}{n_0} = 1.4464(\beta V)^{\frac{1}{2}} \left[1 + \frac{0.2535}{\beta V} - \frac{1}{64} \frac{1}{(\beta V)^2} + \dots \right]$$

For $\beta V \ll 1$, we get

$$\frac{\rho_s}{n_0} = 1 + \frac{\beta V}{\sqrt{\pi}} - (\beta V)^2 + \dots$$

(Expressions are equal for $\beta V = 0.16$.)

Figure 1 is a plot of the stagnation surface density (calculated using the two approximate forms) vs. angle-corrected Mach number, $V \cos \psi / (2e\theta / m)^{1/2}$.

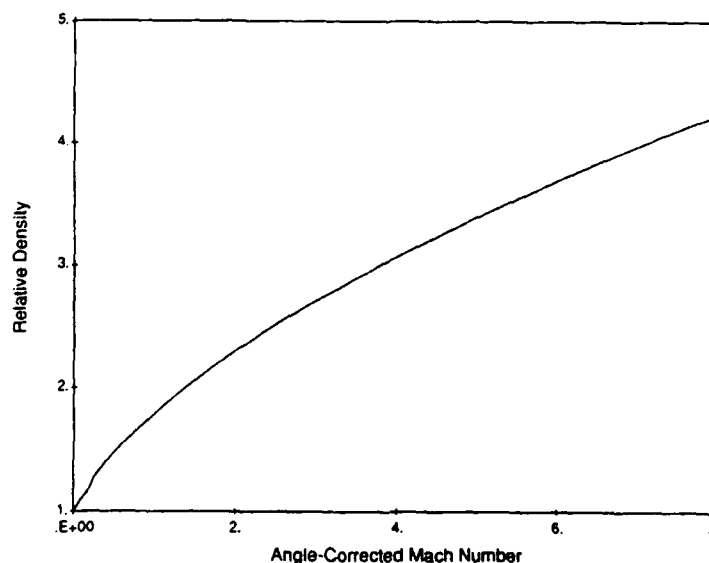
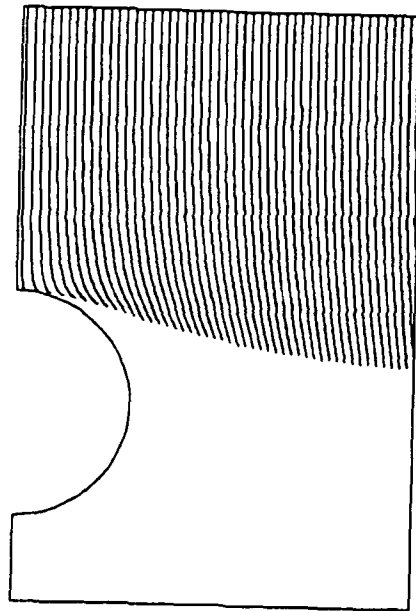


Figure 1. Theoretical estimate of relative density at the stagnation surface vs. angle-corrected Mach number, $V \cos \psi / (2e\theta / m)^{1/2}$.

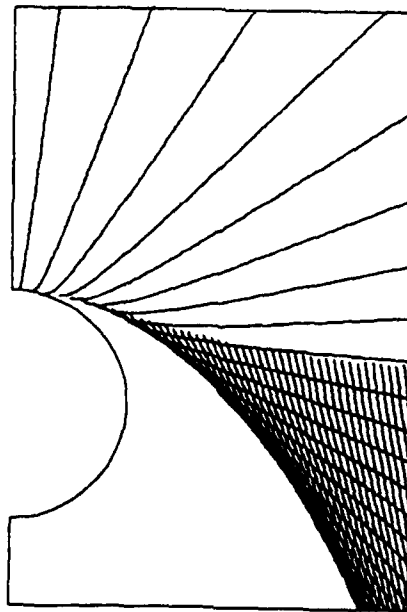
2.3 Particle-Tracking Waterbag Code for Ion Densities

For the purpose of illustrating the stagnation surface and calculating trajectories in the presheath region, we developed a code that tracks cold, constant velocity parallel ions inward in an axisymmetric electrostatic potential. Analysis of these trajectories gives three pieces of information:

1. Inspection of the trajectories shows immediately that space is divided into a region with ions and a region inaccessible to ions, with a sharp stagnation surface. Figure 2 shows the ion trajectories for a coulomb potential. (For reasons to become apparent later, we separate the potential plots into incoming and outgoing portions.)
2. For low impact parameter ions, the point of closest approach is on the stagnation surface. The ratio of the trajectory's initial radius to the closest approach radius gives the factor for density reduction due to trajectory divergence. For the coulomb potential, this ratio is plotted in Figure 3.
3. The number of ions in the volume formed by two adjacent trajectories at two adjacent timesteps is constant. We can obtain the density at a point due to incoming particles by finding the two closest trajectory segments passing to its right and its left, and taking the ratio of the initial segment volume for those trajectories to the segment volume at the point of interest. The density due to outgoing ions can be found similarly. Figure 4 shows the calculated ion density field for the coulomb potential. In doing such a calculation, a maximum density must be set, and an arbitrary grid will make the results appear noisy at the sharp dropoff beyond the stagnation line.



(a)



(b)

Figure 2. Particle trajectories for ram ions incident on a spherical equipotential at the stagnation energy: (a) trajectories up to closest approach to sphere; (b) trajectories beyond closest approach to sphere. The potential field is Laplacian.

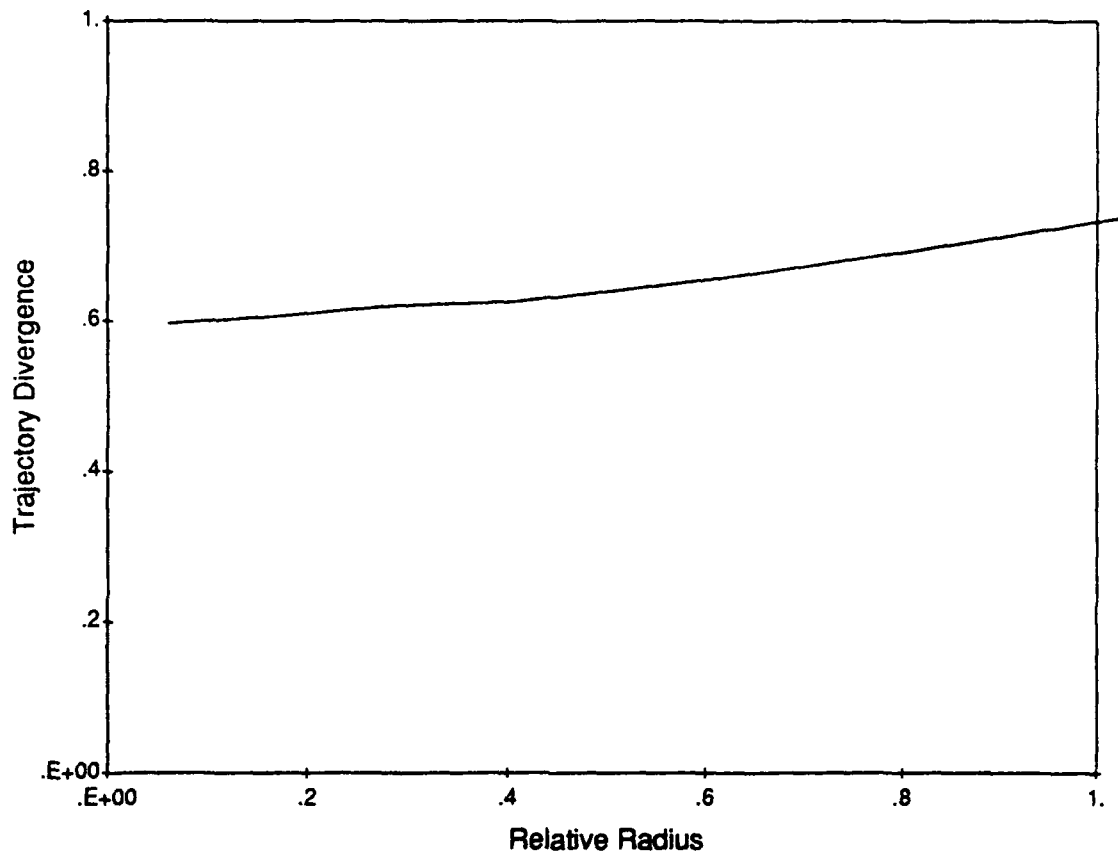


Figure 3. Trajectory divergence in a Laplacian potential. The ordinate is the distance from the symmetry axis divided by the radius of the spherical equipotential at the stagnation energy. The density is reduced by the square of this factor.

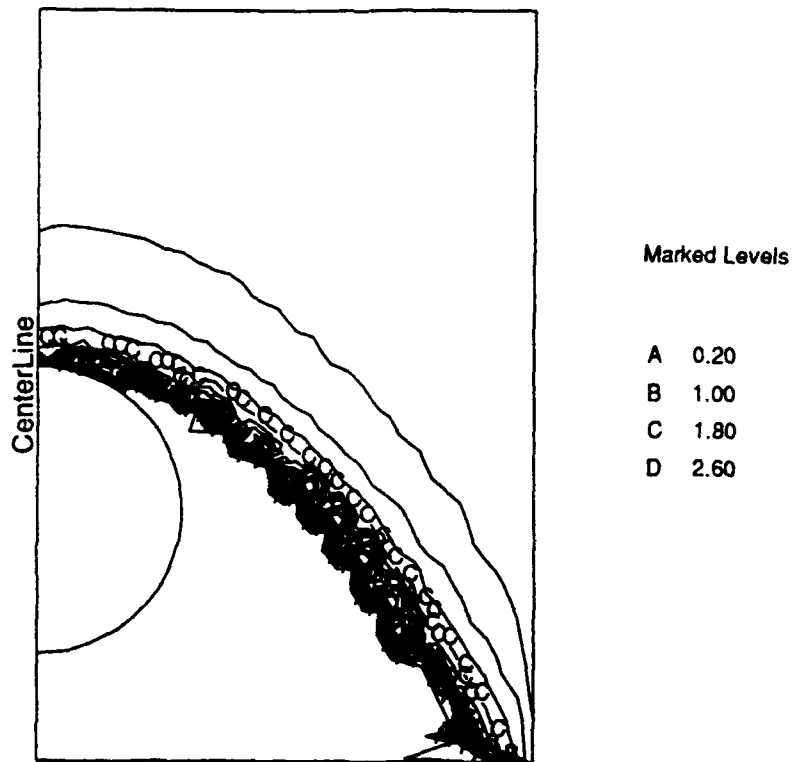


Figure 4. Calculated density contours for ram ions incident on a spherical Laplacian potential. The contour increment is 0.2, with the outermost relative density being 1.2.

2.4 Estimate of Stagnation Surface and Current for a High-Voltage Sphere

If we have a high-voltage sphere (~ 5000 volts), the electrostatic potential must drop to a small value (~ 5 volts) at the stagnation surface due to the space charge associated with the current flowing from the stagnation surface to the probe. If we assume that the current emitted from a segment of the stagnation surface is a function only of its angle, β , relative to the ram, and that the potential structure in the high-voltage region depends only weakly on what assumptions we make governing the presheath region, we can predict the shape of the stagnation surface without explicitly considering the physics or ion dynamics in the presheath region. (Note: In the remaining sections, we use the symbol β for the angle specified as ψ in section 2.)

The calculation proceeds as follows:

1. Construct a spherical, axisymmetric grid such that the grid lines follow lines of constant radius, R , and angle, α .
2. Express the stagnation surface, $R_{\text{stag}}(\alpha)$, as

$$R_{\text{stag}}(\alpha) = a_0 + a_2\alpha^2 + a_4\alpha^4 + a_6\alpha^6$$

$$\partial R_{\text{stag}}(\alpha) / \partial \alpha = 0 \text{ at } \alpha = \pi$$

It follows that

$$\beta(\alpha) = \arctan[(R_{\text{stag}}\sin(\alpha) - \partial R_{\text{stag}} / \partial \alpha \cos(\alpha)) / (R_{\text{stag}}\cos(\alpha) + \partial R_{\text{stag}} / \partial \alpha \sin(\alpha))] .$$

Initially, we choose the stagnation surface as a sphere and set $\beta = \alpha$.

3. Set the charge density in the grid, assuming that current flows radially inward from the stagnation surface. Thus, we have

$$\rho(R, \alpha) = J(\beta) (R_{\text{stag}}(\alpha) / R)^2 \sec(\beta - \alpha) / (2e\phi / m)^{1/2}$$

for points within the stagnation surface. For $\beta < \pi / 2$, we take $J(\beta) = CJ_{th}(N(\beta), \theta(\beta))$. We have taken $C = 1$ (though it can be argued that it should be 2), and $N(\beta)$ as given by the theory above. $\theta(\beta)$ may be taken as $\epsilon \cos^2 \beta / \log (N / N_0)$ or as $\theta_{max} \cos \beta$. For $\beta > \pi / 2$, we take $N(\beta) = N_0 \exp(-V^2)$, where V is the angle-corrected Mach number. Outside the stagnation surface, we assume linear screening with some computationally convenient Debye length (~ 10 cm). (Coincidentally, the total current to the probe can be calculated.)

4. Solve for the electrostatic potential in the grid. For each grid-angle, α for which $\beta(\alpha < \pi / 2)$, find the radius at which the potential drops to $\epsilon \cos^2 \beta(\alpha)$. Fit $R_{stag}(\alpha)$ to these points, and update $\beta(\alpha)$ accordingly. (To achieve convergence, we heavily damp the movement of $R_{stag}(\alpha)$ and $\beta(\alpha)$ from their previous values.)
5. Return to 3.

Figure 5 shows an example of potentials thus calculated. The sphere (1 m in radius) was at 5 kV. We take the ambient density and temperature as

$1 \times 10^{12} \text{ m}^{-3}$ and 0.1 eV. The ram energy, ϵ , was 5 eV, and the stagnation surface temperature was $1 \text{ eV} \times \cos \beta$. The stagnation surface can be seen to extend well wakeward of the sphere. The fitting parameters for the stagnation surface were

$$\begin{aligned} a_0 &= 2.574 \\ a_2 &= 0.07493 \\ a_4 &= 0.09155 \\ a_6 &= -0.00644 \end{aligned}$$

The total current to the sphere was 4.6 amperes.

To get some insight as to the variation of current with problem parameters and comparison with other results, a suite of problems were run using the alternate choice of effective temperature, $\theta(\beta) = \epsilon \cos^2 \beta / \log (N / N_0)$. The results are

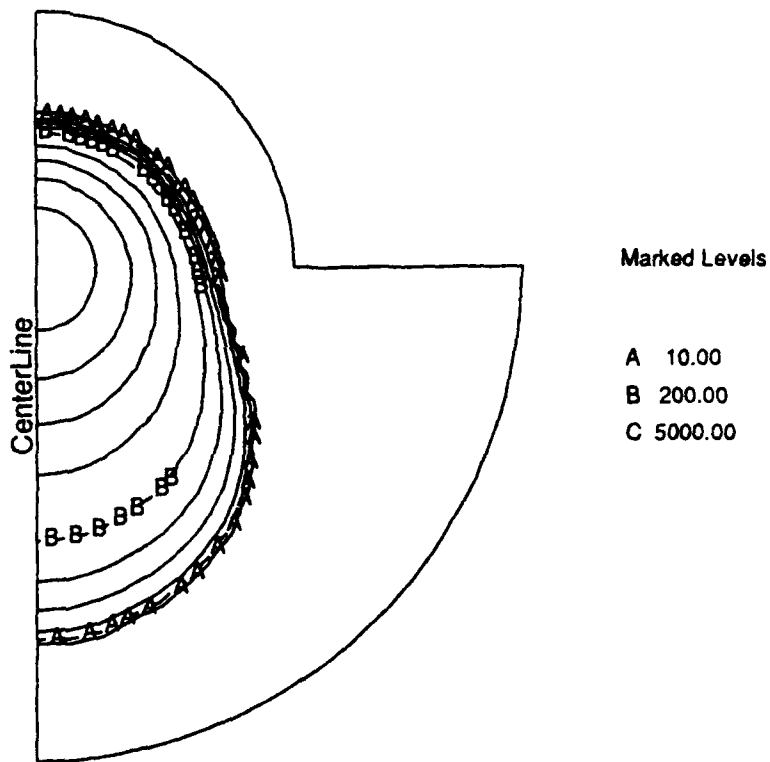


Figure 5. Calculated potential contours for a 5000 volt, 1 m radius sphere in a 5 eV ram plasma. (See text for other computational parameters.) (The negative potential island at center-right is an artifact of the gridding.)

given in Table 1. The 10 cm result is directly comparable to a full PIC calculation that gave a current of 3.84 mA. The 5 cm results are directly comparable to ground test measurements by Lebreton et al. in 1985 (using argon at a velocity of $8 \text{ km} \cdot \text{sec}^{-1}$), which gave results of approximately 7 mA and 2.5 mA. For comparison, the static space-charge-limited currents are 0.7 mA for the 10 cm case, and 2.0 mA and 1.4 mA for the two 5 cm cases. Thus, results calculated by this theory are generally in the range of results obtained by other means and several times the static space-charge-limited current.

Table 1.

Selection of results for calculated electron current to a positively biased orbital probe.

Radius	Potential	N (m ⁻³)	θ (eV)	Current (A)
1 m	5000	1 × 10 ¹²	0.1	6.2
1 m	2000	1 × 10 ¹²	0.1	3.4
1 m	1000	1 × 10 ¹²	0.1	2.4
1 m	5000	1 × 10 ¹²	0.3	4.1
1 m	2000	1 × 10 ¹²	0.3	2.2
1 m	1000	1 × 10 ¹²	0.3	1.6
10 cm	10	1 × 10 ¹¹	0.1	0.0023
5 cm	50	3.4 × 10 ¹¹	0.12	0.0083
5 cm	30	3.4 × 10 ¹¹	0.12	0.0060

2.5 A Model for a Resistive Presheath

Because the temperature and density are both enhanced at the stagnation surface, the current to the probe is well in excess of the ambient plasma thermal current over the same area. Additionally, the presence of a high density of ions within the electron-attracting region requires a means for charge neutralization in order to achieve a quiescent potential structure. Therefore, we postulate that the plasma in this region has sufficient electron scattering and thermalization to maintain quasi-neutrality and can be treated as a resistive medium.

2.5.1 The Current Definition Equation

The current is proportional to the difference between the electric and thermal diffusion forces

$$J = -\sigma \text{ grad } \phi - (\sigma / N) \text{ grad } (\theta N)$$

The conductivity, σ , is given by

$$\sigma = \epsilon_0 \omega_p^2 / \nu$$

and we assume $\nu = \alpha \omega_p$ and further assume $\alpha = 0.51 / 2\pi$. (Later we may allow α to decrease.)

2.5.2 The Equation for the Potential

The equation for the potential is

$$\text{div } J = 0$$

$$- \text{div } \sigma \text{ grad } \phi = - \text{div } (\sigma / N) \text{ grad } (\theta N)$$

2.5.3 The Heat Flux Definition Equation

The heat flux consists of a conductive and a convective portion:

$$Q = - \kappa \text{ grad } \theta - 5/2 J\theta$$

and we take $\kappa = 3/2 \sigma \theta$ in accordance with the Weidemann-Franz law.

2.5.4 The Equation for the Temperature

The equation for the temperature is

$$\text{div } Q = J^2 / \sigma$$

It is convenient to cast this into an equation for θ^2 and multiply by 4/3:

$$- \text{div } \sigma \text{ grad } \theta^2 = 4/3 J^2 / \sigma + 10/3 \text{ div } (J\theta)$$

$$- \text{div } \sigma \text{ grad } \theta^2 = 4/3 J^2 / \sigma - 10/3 \text{ div } [\theta \sigma \text{ grad } \theta - (\theta \sigma / N) \text{ grad } (N\theta)]$$

In addition, we must account for a heat loss of $2 J\theta$ from the inner boundary.

2.5.5 Scaling

Note that, for given fields ϕ , θ , and N , every term in both the potential and temperature equations is proportional to σ . It follows that changing the value of α will scale the current while leaving ϕ and θ unchanged.

Also, each term goes inversely with the square of the characteristic distance in the problem. Thus, if the linear size of the problem is decreased by a factor of

10, the potential and temperature contour plots will appear unchanged, but the current will be increased by a factor of 10.

2.5.6 Finite Element Solution

The potential and temperature equations are of the form required to use the finite-element method. The matrix for

$$-\int dV \operatorname{div} \sigma \operatorname{grad} \phi$$

is the matrix for

$$\int dV \sigma |\operatorname{grad} \phi|^2 .$$

This allows us to construct the matrix of equations corresponding to the left-hand side and the operators needed to evaluate the right-hand side. We use ICCG to alternately solve the potential and temperature equations, with the right-hand sides calculated using existing values. To obtain convergence, after solving for θ^2 we mix a small fraction of the new temperature with the old temperature and run many iterations.

2.5.7 Defining a Problem

The following sequence defines a problem:

1. Define a grid for the region in which the above equations are expected to hold. The region's outer boundary will be fixed to constant (ambient) potential and temperature. The inner boundary is fixed in potential (not necessarily constant).
2. Define a quasi-neutral density, N , throughout the region. Define initial potentials (e.g., Laplacian) and initial temperatures (e.g., constant).
3. The density is assumed to drop abruptly to zero (i.e., the medium becomes collisionless) beyond the inner boundary. Convective heat loss through the boundary is subtracted from the right-hand side of the temperature equation. The total current through the inner boundary is computed.
4. The current should be consistent with the thermal current characterizing the final density and temperature at the inner boundary. This result can be achieved by adjusting α .

2.5.8 Example 1: A Spherical Stagnation Surface

As a preliminary example, we did a sphericalized version of a probe in a flowing plasma. We constructed an axisymmetric grid (Figure 6) representing the space around a sphere with radius 2.3 m. The sphere was set at $\phi = 5$ volts and the outer boundary at $\phi = 0$ volts and $\theta = 0.1$ eV. We solved for Laplacian potentials, ϕ_L , and set the densities by

$$N / N_0 = [5.5 / (5.5 - \phi_L)]^{1/2}$$

which gave a relative density at the sphere surface of 3.32. The ambient density, N_0 , was set to 10^{12} m^{-3} . The potential and temperature equations were solved, leading to the contours shown in Figures 7 and 8. The total current was 1.77 amperes, and the temperature at the sphere surface was 0.95 amperes.

The calculated total current should be compared with the total thermal current over a spherical surface at the density and temperature used here. For this case, the total thermal current is 5.78 amperes, more than three times the calculated current. This suggests that the scattering parameter, α , should be reduced by about a factor of three. In reality, α should not be a constant. One class of model would be that α is a function of the local current and thermal current, increasing

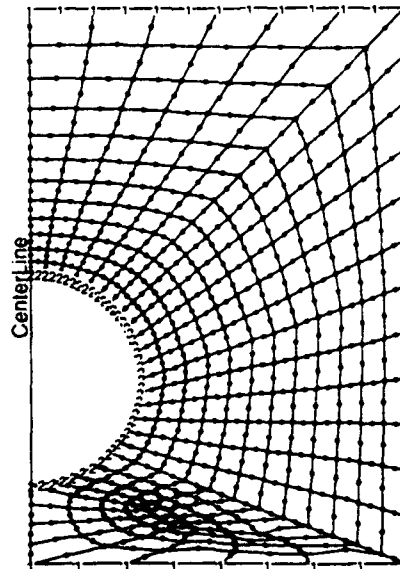


Figure 6. Axisymmetric finite element grid used for spherical stagnation surface example. The grid is composed of biquadratic elements. Symbols "1" and "2" label the outer (ambient) and inner (stagnation) boundaries, respectively.

sharply as the current reaches the thermal current. Such a scattering parameter model would tend to produce the local thermal current at the stagnation surface.

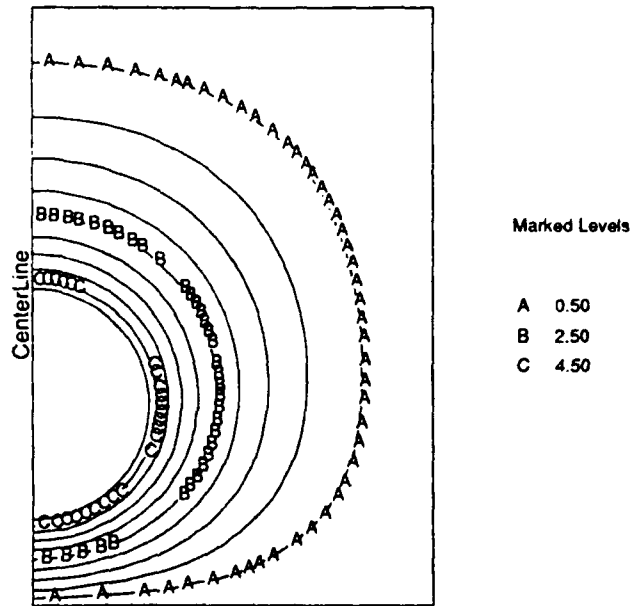


Figure 7. Calculated equipotential contours for the spherical stagnation surface example. The contour increment is 0.5 volts.

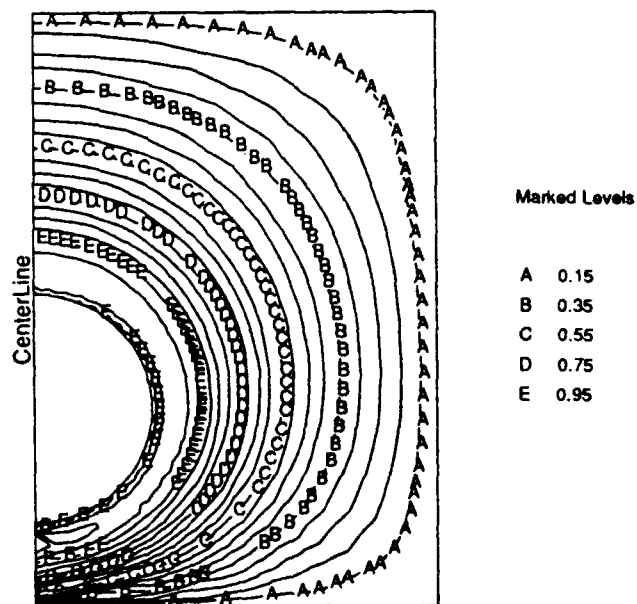


Figure 8. Calculated equithermal contours for the spherical stagnation surface example. The contour increment is 0.05 eV. A broad temperature maximum of about 1 eV appears outside the stagnation surface.

2.5.9 Example 2: A Realistic Stagnation Surface

Now, we are prepared to solve the resistive presheath problem for the stagnation surface calculated above with the model for the high-field sheath region. We proceeded as follows:

1. The fit to the stagnation surface calculated in section 4 was used to construct points on the stagnation surface from $\alpha = 0$ to $\alpha = 2$. The surface was extended by hand to a plane 4 m wakeward of the cube center.
2. An axisymmetric grid (Figure 9) was constructed exterior to the stagnation surface. The boundary conditions on the exterior grid boundary are

$$\theta = 0.1 \text{ eV and } \phi = 0.$$

3. Potentials on the stagnation surface were set to $\max(0.1, \epsilon \cos^2 \beta)$ ($\epsilon = 5 \text{ eV}$), and Laplace's equation was solved in the grid.
4. Relative densities at the grid points were set to $\min(n_{\text{stag}}, (\epsilon / (\epsilon - \phi))^{1/2})$, where n_{stag} is the stagnation surface density for $\beta = \cos^{-1} (\phi / \epsilon)^{1/2}$. This gives a density field that is smooth and reasonable but neither strictly correct nor strictly consistent with the sheath region calculation leading to the stagnation surface. Figure 10 shows the resulting density contours.
5. The resistive presheath model was run, leading to potential and temperature fields shown in Figures 11 and 12. We see that there is a large region of 1 eV temperature near the "nose" of the stagnation surface, and both the potential and temperature fields are long-ranged.

As with the spherical model for a similar scale problem, we expect that the calculated current will be less than the thermal current integrated over the stagnation surface. In this case, the two currents were 0.34 and 2.6 amperes, respectively, suggesting that we have overestimated the scattering parameter, α , by about a factor of eight. (Note that the integrated thermal current is well below that calculated in the earlier model, primarily because the stagnation surface density was set below n_{stag} for $\beta > 15^\circ$.)

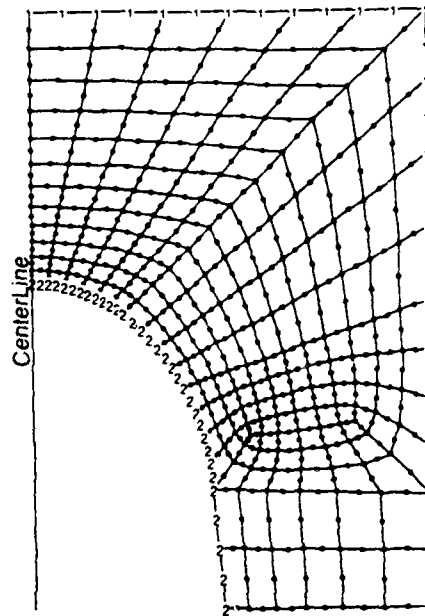


Figure 9. Axisymmetric finite-element grid used for studying the presheath outside a realistic stagnation surface. The stagnation surface (marked "2") is based on the parameters quoted in the previous section. The grid extends 4 m wakeward, 8 m ramward, and 8 m outward, from the center of a 1 m radius sphere (not show) at 5 kV.

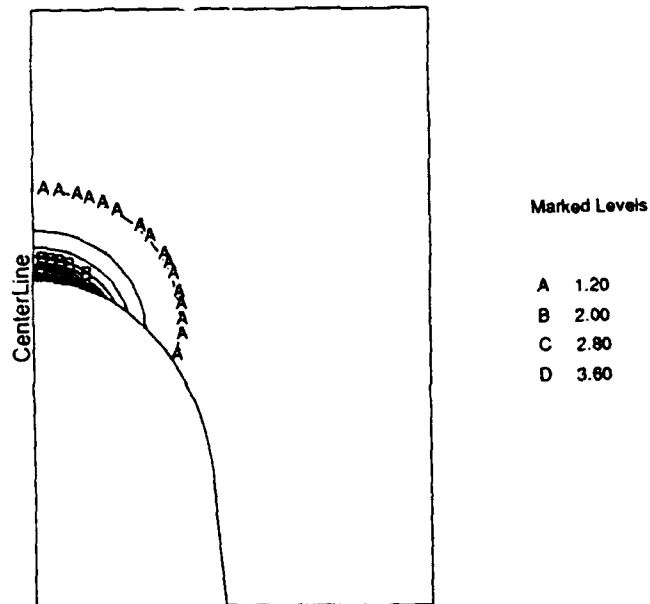


Figure 10. Assumed ion density contours (computed as described in the text) outside the stagnation surface.

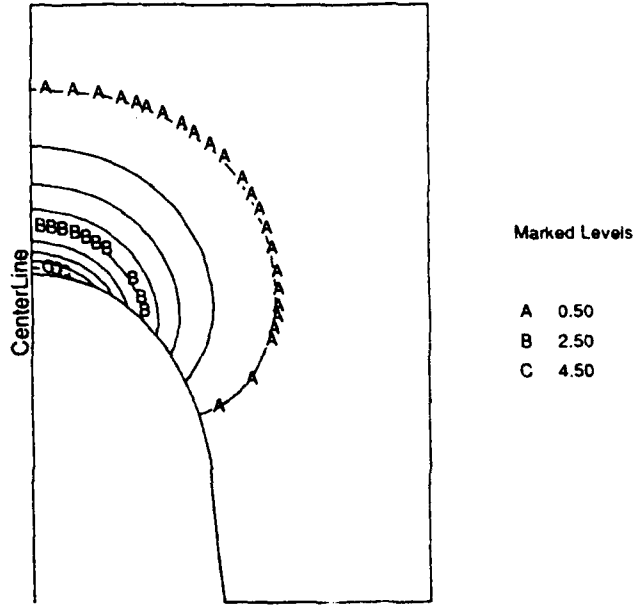


Figure 11. Calculated equipotential contours in the resistive presheath.

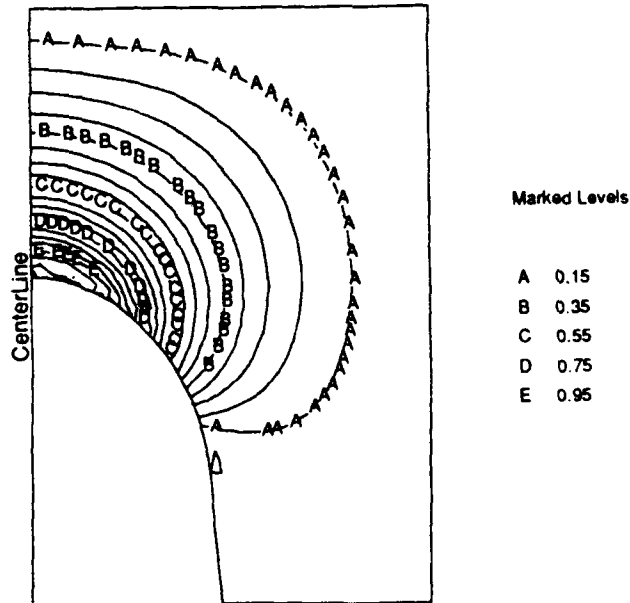


Figure 12. Calculated equithermal contours in the resistive presheath.

The next logical step would be to set ion densities consistent with the calculated potentials and rerun the resistive model. This was not done, in part, because it is believed that the model is reasonably insensitive to the precise density values and, in part, because our faith in the theory is not sufficient to justify the additional effort. However, it is satisfying to close the problem by calculating "waterbag" trajectories and densities in the final potentials. These are shown in Figures 13 and 14. It is seen that the proposed stagnation surface is not too far off from that shown by the particle trajectories, with the actual stagnation surface being wider in the wake region. The trajectory divergence (Figure 15) indicates a factor of two drop in density (relative to the theoretical result we have used) at the nose of the stagnation surface. Also, note that (ignoring the noise right on the stagnation line) the density enhancement profile in front of the stagnation surface appears fairly uniform.

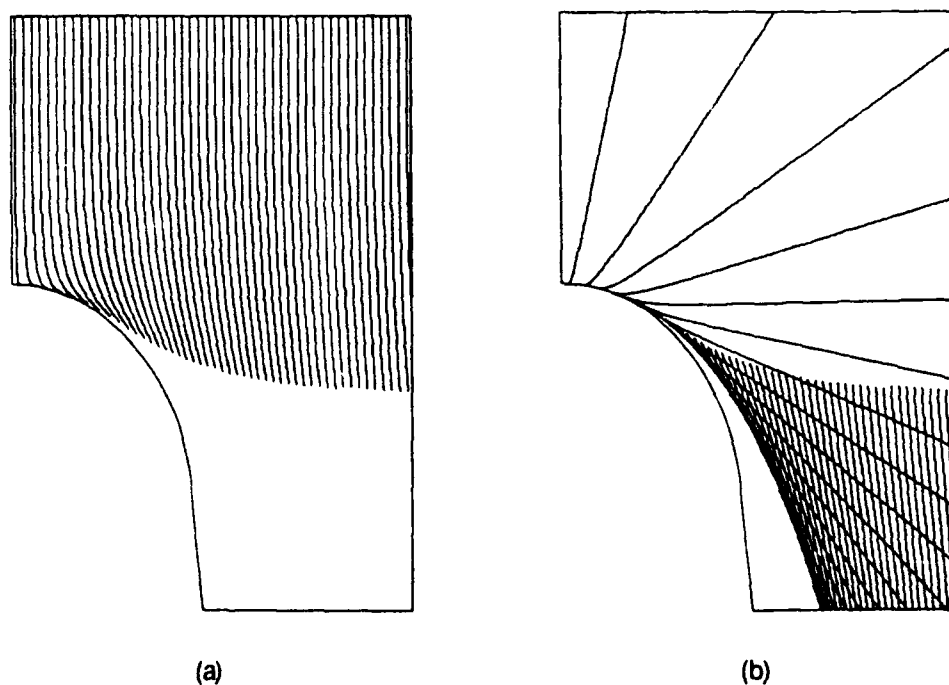


Figure 13. Particle trajectories for ram ions incident on the resistive presheath potentials shown in Figure 11: (a) trajectories up to closest approach to sphere; (b) trajectories beyond closest approach to sphere.

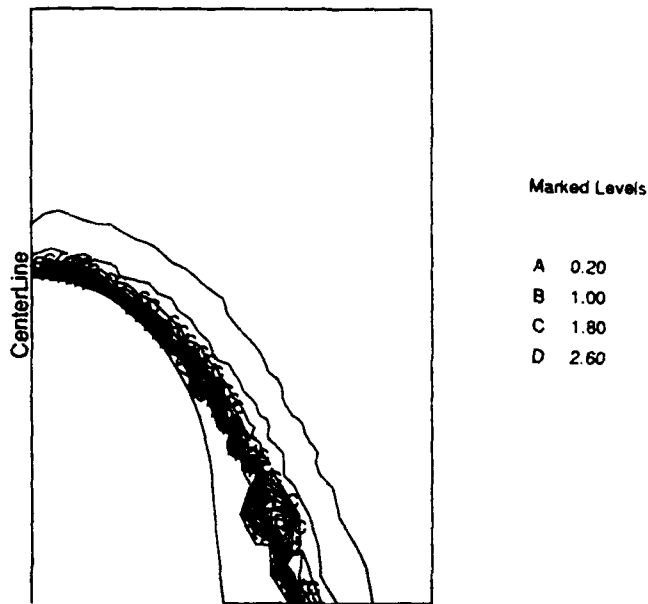


Figure 14. Relative ion densities calculated from the trajectories shown in Figure 13.

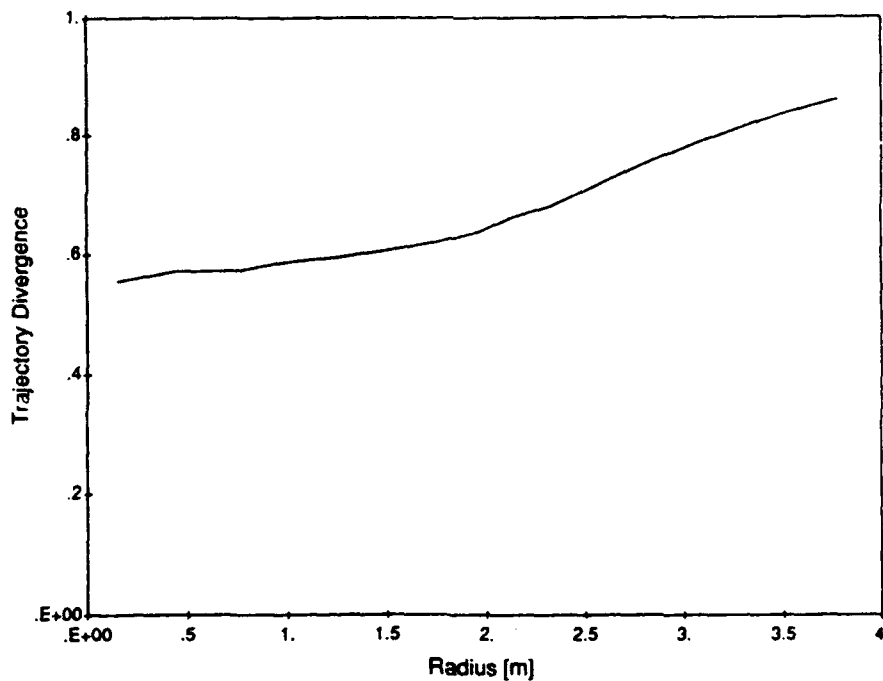


Figure 15. Trajectory divergence for the trajectories of Figure 13, as a function of distance from the symmetry axis. (Compare with Figure 3.)

3. CONSISTENT SOLUTION FOR CURRENT TO ORBITAL PROBE

In the previous report, we approached the calculation of the current and sheath structure about a probe such as the TSS-1 satellite from several points of view. First, we showed that the shape of the ion stagnation surface in the ram direction and its distance from the probe can be estimated by a sheath calculation that takes account of the space charge due to current drawn from the stagnation surface and collected by the probe. The calculation requires models for the density and temperature at the stagnation surface and predicts the collected current. Second, we showed that, in the limit of strong electrostatic scattering (resistive limit), we can calculate potentials and temperatures external to the stagnation surface. This calculation requires models for the plasma electrical and thermal conductivities, the location and potential of the stagnation surface, and ion density values external to it. With the models chosen, the temperature and density fields were independent of the scattering rate coefficient, so that this coefficient could be determined by equating the resistive model current to the plasma thermal current through the stagnation surface. Finally, we could track ram ions to determine if the supposed stagnation surface was consistent with the potentials predicted by the resistive presheath model.

The above calculations used ion densities predicted with a theory that took account of thermal spreading but assumed a short-range potential. The predicted presheath potentials were long-ranged (similar to Laplacian or coulombic) in nature, which prompted the investigation into coulomb potential ion densities during this report period. It was found that, for the Mach-number range of interest, very little ion density enhancement actually took place, with the peak densities being only ~30 percent above ambient.

Consequently, we proceeded to calculate a solution that was consistent in the following senses:

1. The ion density was taken to be equal to the ambient density, which is reasonably adequate for a long-range potential and realistic Mach-number.

2. The stagnation surface temperature used in the sheath calculation was consistent with the predictions of the resistive presheath.
3. The distance of the stagnation surface from the probe was determined by the sheath calculation.
4. The stagnation surface was taken to be a parabola, with curvature chosen to make it reasonably consistent with trajectory calculations.
5. The potential of the stagnation surface was taken as $\epsilon \cos^2\beta$ (with ϵ the ram energy and β the angle between the surface normal and the ram), which is correct both for a short-range potential and for the coulomb potential.

The problem parameters were the same as in the previous report: a sphere 1 m in radius at a potential of 5000 V, orbiting in an O⁺ plasma of density 10^{12} m^{-3} and temperature of 0.1 eV. The ram energy is 5 eV, and the Mach number is about 7.

Figure 16 shows the results for the interior sheath calculation. The stagnation surface temperature was taken as

$$\theta_s = 0.061 + 0.103 \cos\beta + 1.411 \cos^2\beta$$

The distance of the stagnation surface from the probe center was found to be

$$R_s = 2.776 + .09685 \alpha^2 + .06815 \alpha^4 - .004936 \alpha^6$$

where α is the actual polar angle. The current was predicted to be 3.5 amperes.

Figure 17 shows the calculated temperature and density fields in the presheath. The presheath surface was taken as a parabola given by

$$z = 2.776 - 0.24584 r^2$$

in cylindrical coordinates. (For comparison, the stagnation surface for a coulomb potential centered at the probe would be $z = 2.776 - 0.09 r^2$.) The predicted stagnation surface temperature was

$$\theta_s = 0.039 + 0.276 \cos\beta + 1.241 \cos^2\beta ,$$

which is adequately close to the expression used in the inner sheath calculation. The resistive current was calculated as 0.45 amperes, while the total thermal current was 3.25 amperes (indicating that the standard scattering coefficient was a factor of 7 too high).

Figure 18 shows the ion trajectories in the calculated potentials, indicating reasonable consistency between the ion trajectories and the assumed stagnation surface.

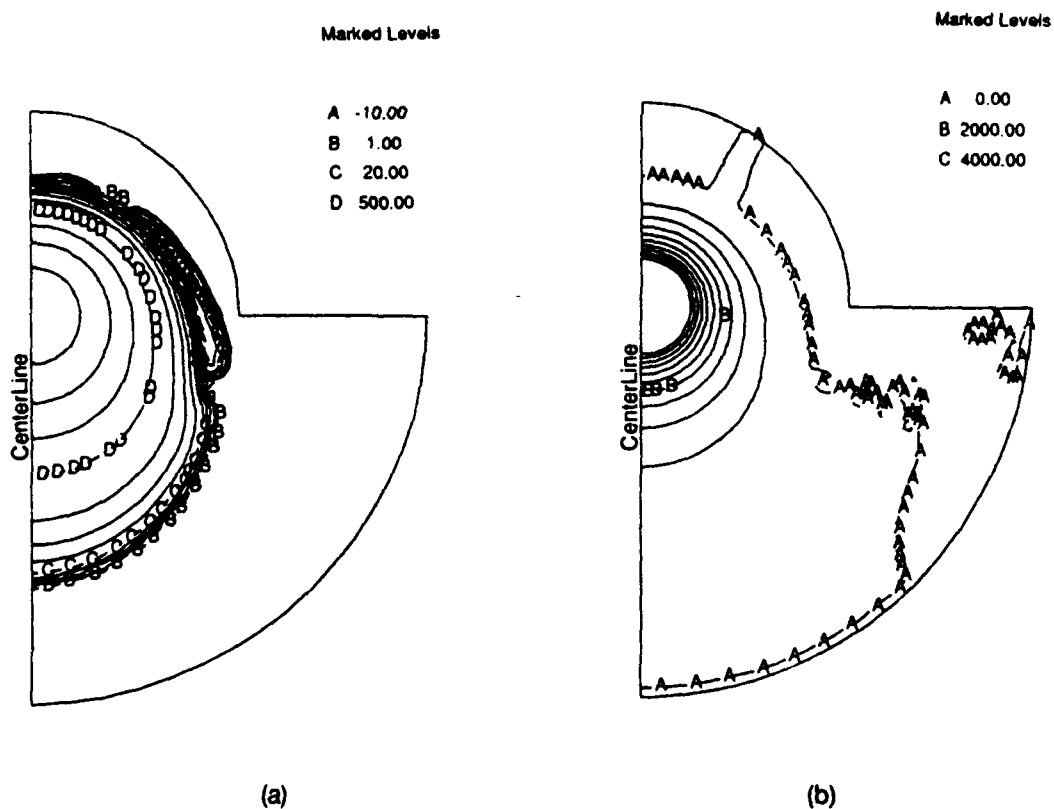
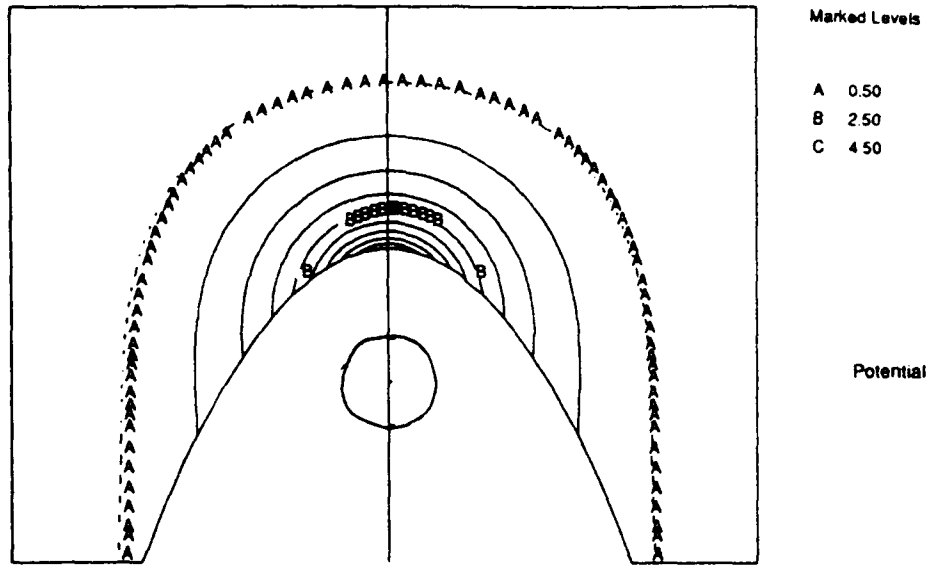
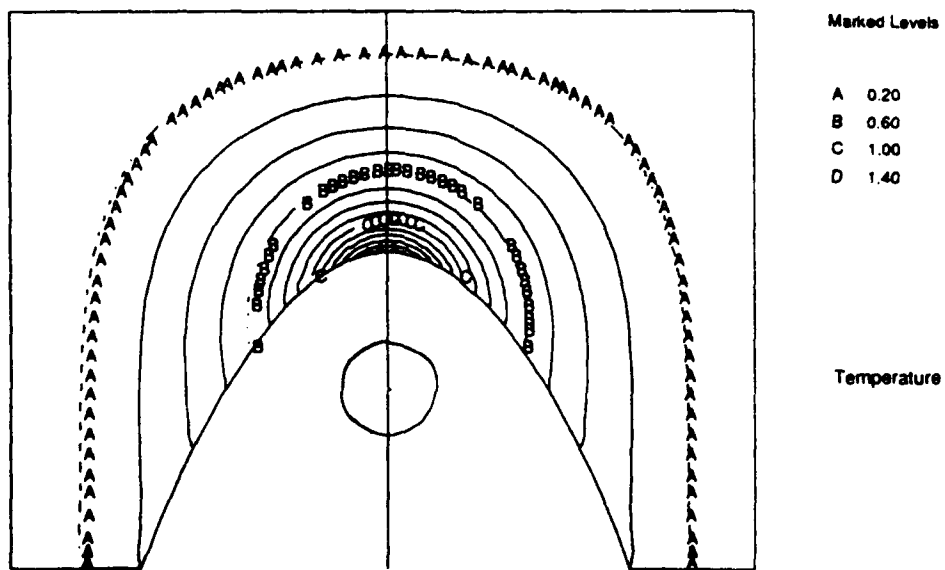


Figure 16. Potentials about the moving probe calculated using the inner sheath model: (a) logarithmically spaced contours; (b) uniformly spaced contours.



(a)



(b)

Figure 17. Potentials (a) and temperatures (b) in the presheath calculated using the resistive presheath model.

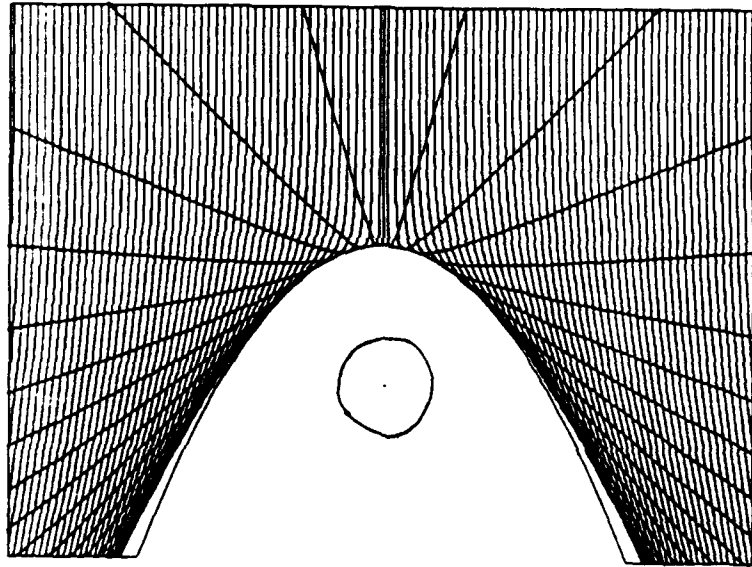


Figure 18. Ion trajectories in the potentials of Figure 17.

4. ION STAGNATION IN A REPULSIVE COULOMB POTENTIAL

4.1 Introduction

To gain some insight into the peak density and density structure of ions near a positively charged body in ionospheric orbit, we have studied the tractable problem of stagnation in a coulomb potential. The coulomb field is a representative long-ranged potential. While we do not ordinarily expect charged bodies to have long-ranged potentials under ionospheric conditions, the penetration of ram ions (at 5 eV energy) well inside the electron-collecting sheath leads to a fundamentally unstable situation, which may resolve itself by a long-ranged presheath potential. For example, if we suppose the presheath to be quasi-neutral and resistive, the potential is determined by $\text{div } \mathbf{J} = 0$, leading to a field similar to the coulomb field.

The plan of development is as follows:

1. For zero temperature (or infinite Mach number) we define and determine the stagnation surface.
2. We calculate the density along the symmetry axis for infinite Mach number, and with thermal spread in the orbital direction only. (It is also possible to calculate approximately the density near the stagnation surface with thermal spread in the orbital direction only.)
3. We write the equations for the density at an arbitrary point with infinite Mach number and calculate the density field for various finite Mach numbers.

4.2 Nomenclature

We will try to consistently maintain the following symbols in the development:

r, z	Cylindrical coordinates, with z in the orbital direction $(r^2 + z^2)^{-1/2}$
V	The negative of the orbital velocity
ϵ	Energy of ion (eV)
ϵ_0	Energy of ion with velocity V
ψ	$\arccos(uz)$
a	Radius of equipotential ϵ , with $a_0 = 1$ the radius of equipotential ϵ_0
r_0	Initial ($z = \infty$) value of r for a particle trajectory
ρ	Local density (relative to ambient)
θ	Plasma temperature (eV)
M	Mach number, $(\epsilon_0/\theta)^{1/2}$

4.3 Stagnation Surface at Zero Temperature

The stagnation surface is the surface at which incoming orbits change to outgoing orbits. An orbit can be identified as incoming or outgoing by a neighboring orbit of slightly higher angular momentum being on its left or on its right. The stagnation surface is therefore the surface at which infinitesimally close orbits cross.

We start with the equation above (3-46) of Goldstein,¹ which, for incoming orbits parallel to the z -axis, can be written

$$\psi = - \arccos [-a / (a^2 + 4r_0^2)^{1/2}] \pm \arccos [-a + 2ur_0^2] / (a^2 + 4r_0^2)^{1/2}$$

where the \pm divides the orbit at closest approach to the center of potential (maximum value of u). Neighboring orbits cross when $\partial\psi/\partial r_0 = 0$ for fixed u . The equation for the stagnation surface is thus

$$0 = a\partial\psi/\partial r_0 = [2a^2/(a^2 + 4r_0^2)] \pm 2(1 - au - r_0^2u^2)^{-1/2}[au - (1 + 2r_0^2u/a) / (1 + 4r_0^2/a^2)]$$

whose solution is

$$u = a / (a^2 + r_0^2)$$

$$r = 2r_0$$

$$z = a(1 + r_0^2/a^2) = a(1 + r^2/4a^2)$$

Thus, the stagnation surface is a parabola. Figure 19 shows numerically calculated orbits for a coulomb potential. The orbit crossing structure shown in Figure 19(a) becomes simplified when the orbits are divided at the stagnation surface into incoming [Figure 19(b)] and outgoing (Figure 19(c)) portions.

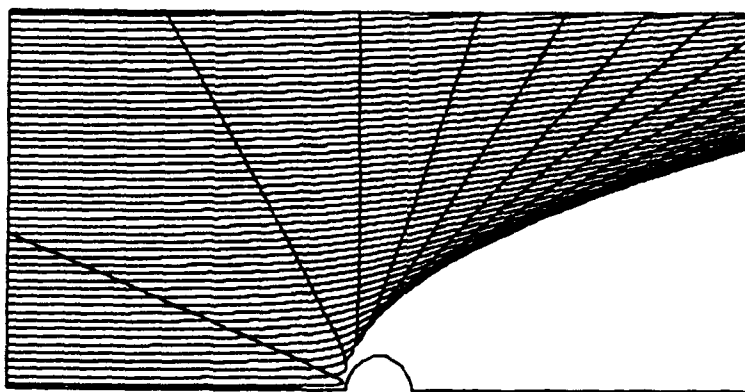


Figure 19(a). Ram ion trajectories in a coulomb potential, showing trajectory crossings.

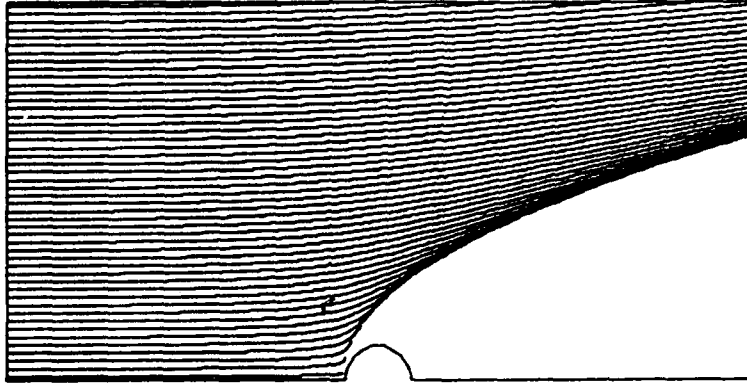


Figure 19(b). Incoming portion of the trajectories of Figure 19(a).

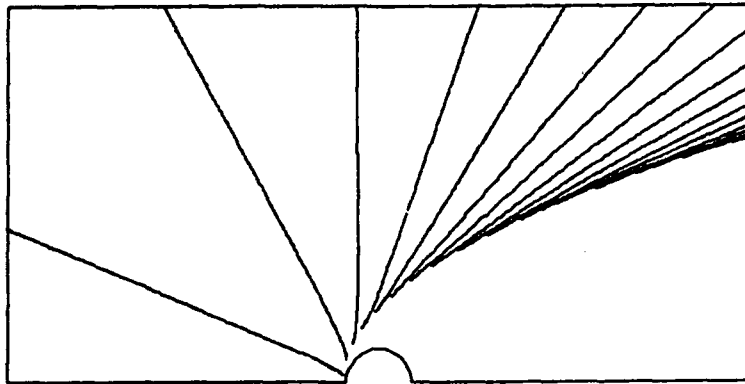


Figure 19(c). Outgoing portion of the trajectories of Figure 19(a).

4.4 Density Along the Symmetry Axis

We start out with one trajectory being well-known: a particle coming in exactly along the symmetry axis will slow down, turn around, and exit along the symmetry axis, traversing a trajectory $(r,z) = [0, z_0(t)]$. A particle coming in slightly off (by distance δ) the symmetry axis will execute a trajectory $(r,z) = [w(t)\delta, z_0(t)]$, with $w(-\infty) = 1$ and $w(0) = 2$. The density along the axis will then be

$$\rho(0,z) = (1 - \epsilon_0 a_0 / \epsilon z)^{-1/2} (w_-(z)^{-2} + w_+(z)^{-2})$$

where w_{\pm} are the values of w for the incoming and outgoing portions of the trajectory. The density then follows immediately from finding the function $w(z)$.

First, we find the relation between $z(t)$ (dropping the "0" subscript) and t :

$$dz/dt = \pm [(2e/m)(\epsilon - \epsilon_0 a_0 / z)]^{1/2}$$

$$(\epsilon z^2 - \epsilon_0 a_0 z)^{-1/2} z dz = \pm (2e/m)^{1/2} dt$$

$$[\epsilon z(\epsilon z - \epsilon_0 a_0)]^{1/2} + \epsilon_0 a_0 \log [(\epsilon z / \epsilon_0 a_0)^{1/2} + (\epsilon z / \epsilon_0 a_0 - 1)^{1/2}] = \pm (2e\epsilon/m)^{1/2} \epsilon t$$

By considering the radial acceleration by the coulomb field, we find that the function $w[z(t)]$ satisfies the equation

$$w[z(t)] = 1 + \int_{-\infty}^t dt_1 \int_{-\infty}^{t_1} dt_2 (e/m) a_0 \epsilon_0 w[z(t_2)] z^{-3}(t_2)$$

which, by changing the order of integration, can be written as a single integral

$$w[z(t)] = 1 + \int_{-\infty}^t dt_2 (t - t_2) (e/m) a_0 \epsilon_0 w[z(t_2)] z^{-3}(t_2)$$

Since we have already expressed t and dt in terms of z and dz , $w(z)$ is readily found by integrating along the trajectory. The function $w(z)$ is shown in Figure 20. Finally, the density $\rho(0,z)$ can be constructed.

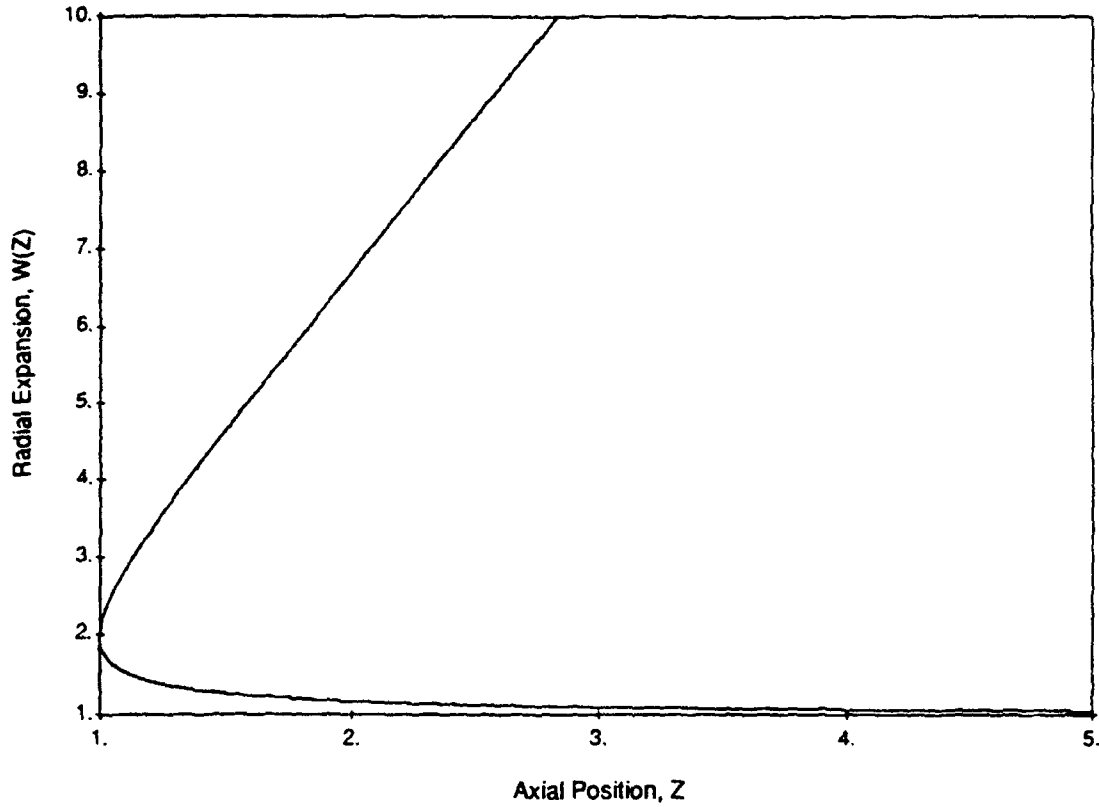


Figure 20. The function $w(z)$, giving trajectory spread along the symmetry axis. Lower branch is for incoming trajectories, and upper branch for outgoing trajectories.

If we know the density along the axis, $\rho_0(0,z)$ for ions of energy ϵ_0 , the density for ions of energy ϵ is given by

$$\rho_\epsilon(0,z) = \rho_0(0, \epsilon z / \epsilon_0) .$$

The density at a point z on the axis is then obtained by integrating over the ambient velocity distribution, leading to

$$\rho(0,z) = (\pi^{-1/2}) \int_{Mz^{-1/2}}^{\infty} dv \rho_{v^2\theta}(0,z) e^{-(v-M)^2} .$$

Figure 21 shows the density along the axis for zero temperature (infinite Mach number) and for Mach number $M = 7$. It is seen that the finite temperature case has a broad density peak at the relatively modest value of 1.3, and that this peak occurs well beyond the stagnation point. Also, there is substantial ion density within the stagnation point.

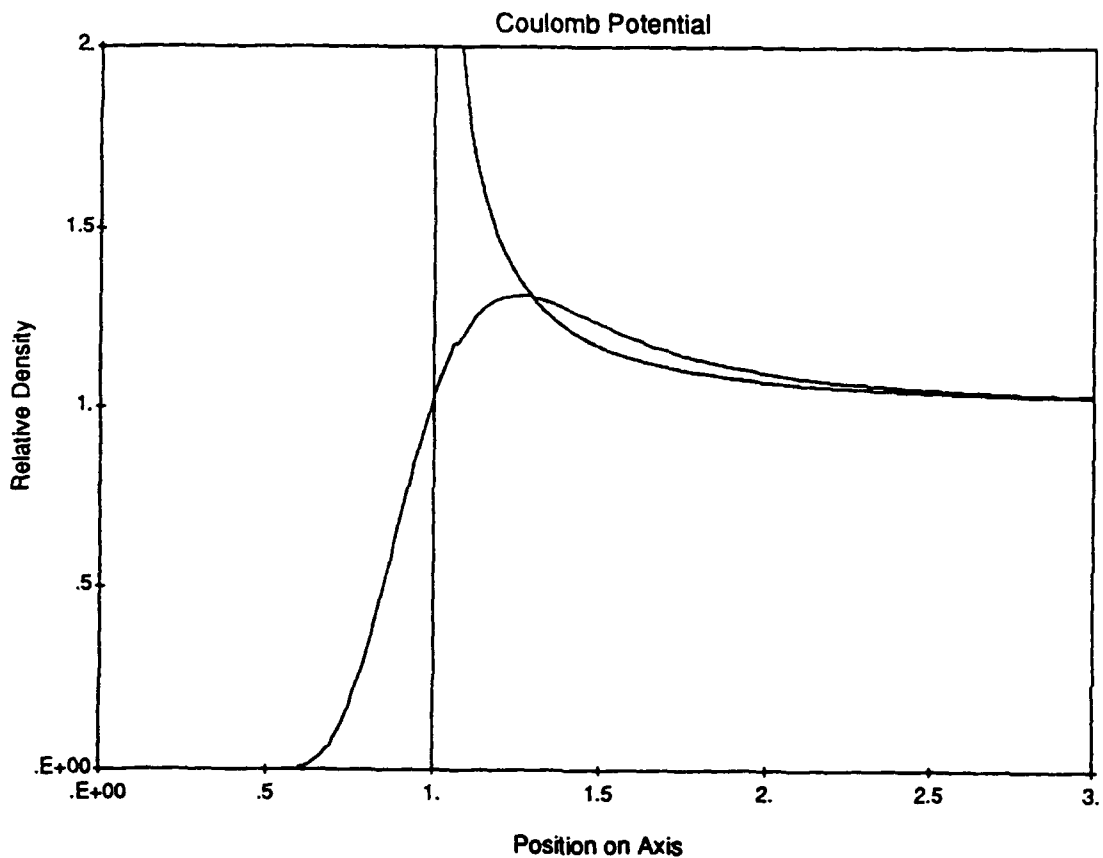


Figure 21. Density along the symmetry axis for Mach 7 (broad curve) and Mach ∞ (sharply peaked curve).

4.5 Density at an Arbitrary Point

The orbit equation allows us to solve (at least in principle) for the origination radii, r_0 , of the incoming and outgoing orbits at an arbitrary point $(r,z) = (r \sin\psi/u, r \cos\psi/u)$. The separation between two orbits originally separated by dr_0 is $dr_0 |\nabla r_0|$, and

$$\nabla r_0 = (-u^2 \partial r_0 / \partial u, u \partial r_0 / \partial \psi) .$$

(Note that, since an orbit is a path of constant r_0 , ∇r_0 is necessarily perpendicular to the orbit.) Thus, the density at a point is given by

$$\rho_\varepsilon(r,z) = (1 - au)^{-1/2} (r_0/r) |\nabla r_0| .$$

By taking the cosine of the orbit equation, it is simplified somewhat to

$$0 = a^2(1 - \cos\psi) - 4r_0^2[\cos\psi \pm (1 - au - u^2r_0^2)^{1/2}] + 2uar_0^2 .$$

This equation is solved numerically for r_0^2 , (and thus r_0) and will have either (1) two roots for the "+" branch, (2) one root for each branch, or (3) no roots. Once r_0 is known, differentiating the equation by u or by ψ gives a linear equation for the derivatives required to find ∇r_0 . (Note: it appears numerically that the density contribution from incoming ions exceeds that from outgoing ions by exactly the ambient density.)

To find the density for the finite Mach number, we must integrate over the thermal velocity distribution, which is a 3-dimensional gaussian about the ram velocity. For each point in velocity space, we rotate the coordinate system so that the z axis is parallel to the particle velocity, giving a transformed polar angle, ψ' , of

$$\begin{aligned} (v_x^2 + v_z^2)^{1/2} \cos\psi' &= v_z \cos\psi + v_x \sin\psi \cos\phi \\ (0 < \phi < 2\pi) \end{aligned}$$

where v_x and v_z are the velocity components perpendicular and parallel to the ram direction. After de-dimensionalizing, the entire expression becomes

$$\pi^{3/2} \rho(r,z) = \int_{-\infty}^{\infty} dv_z e^{-(v_z - M)^2} \int_0^{\infty} v_x dv_x e^{-v_x^2} \int_0^{\pi} d\phi \rho_{\varepsilon}(u, \psi')$$

$$\varepsilon = (v_x^2 + v_z^2)\theta$$

Figure 22 shows a sequence of ion density contour plots for various Mach numbers. For Mach 1, we can still see remnants of the spherical Mach 0 case, with contours of substantial density closing in the near wake. By Mach 3, the stagnation structure has become very recognizable, but there is no peak in the ion density. At Mach 7, the ion density shows a broad maximum of about 1.3, with the peak density occurring well outside the stagnation line. With further increase in Mach number, the density gradients tighten around the stagnation line, with modest rise in the peak density. The peak density rises to about 2.3 at Mach 30 and about 4.1 at Mach 100.

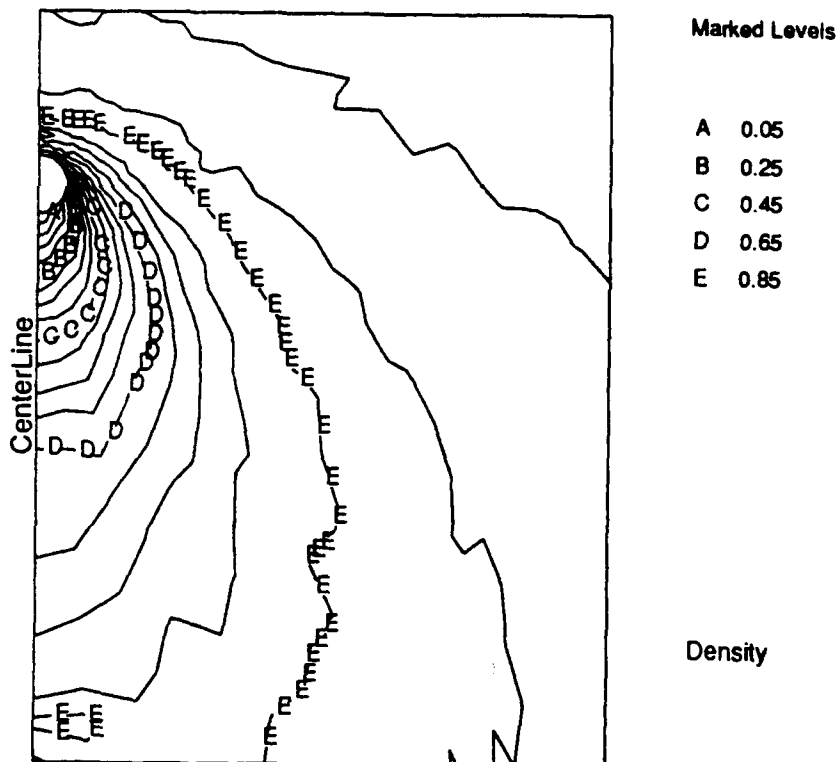


Figure 22(a). Ion densities for Mach 1. The boundaries of the figure are $0 < r < 10a_0$ and $-10 < z/a_0 < 3$, with an excluded sphere of radius $0.5a_0$.

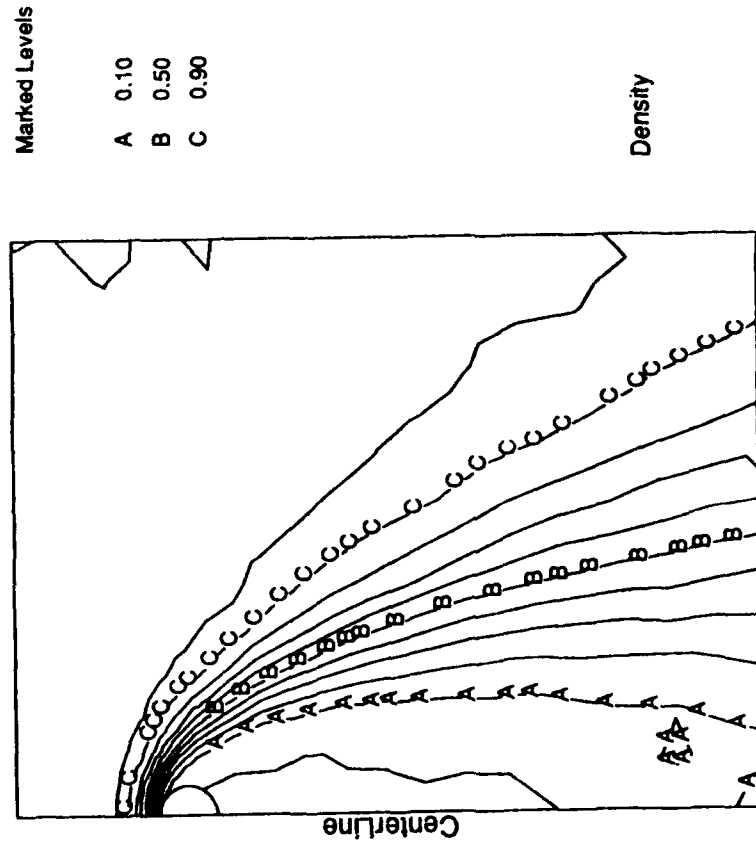


Figure 22(b). Ion densities for Mach 3.

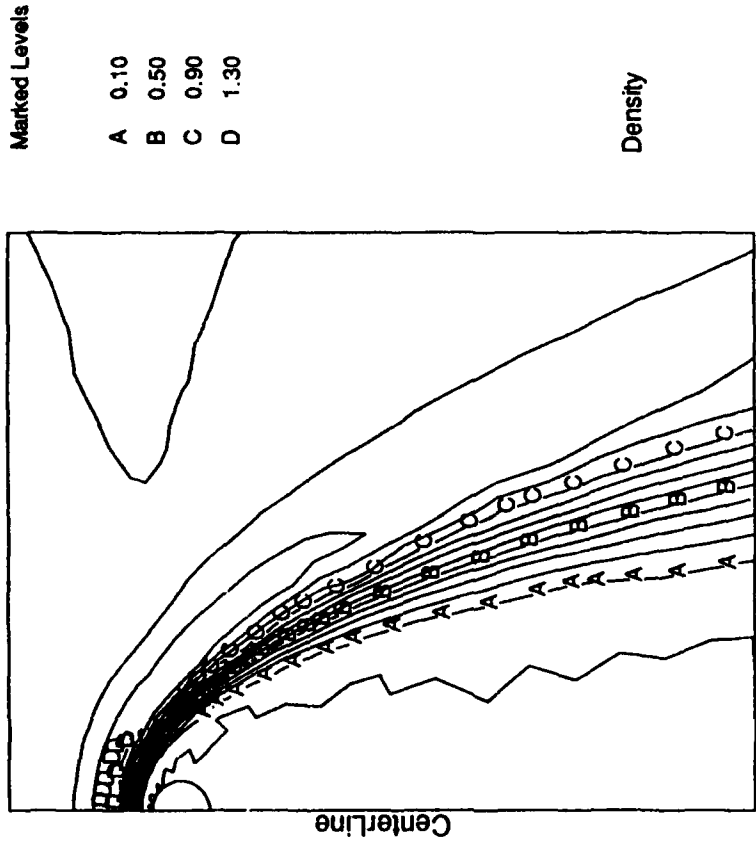


Figure 22(c). Ion densities for Mach 7.

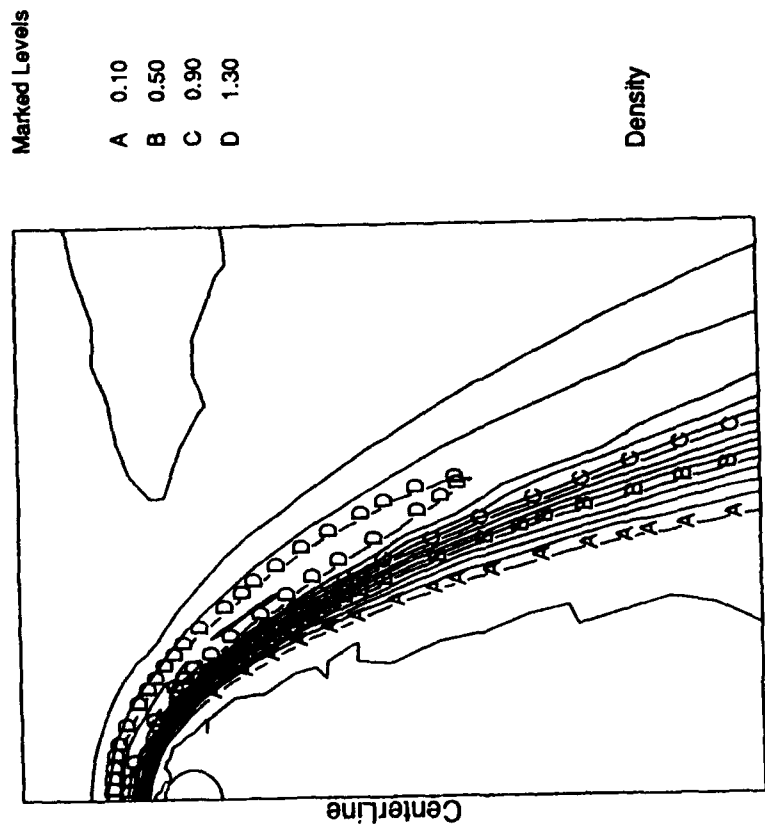


Figure 22(d). Ion densities for Mach 10.

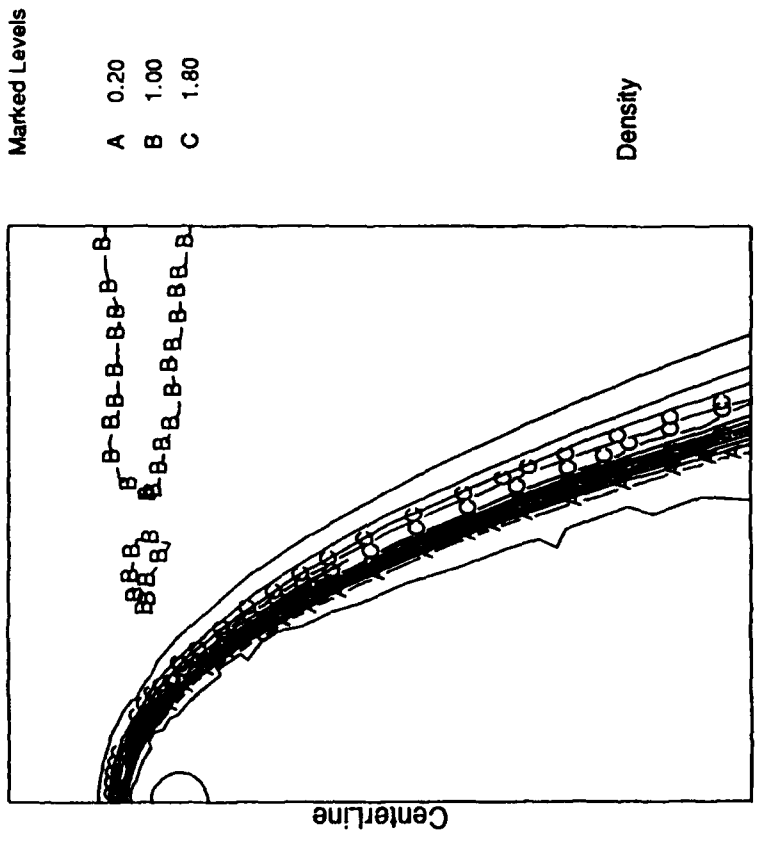
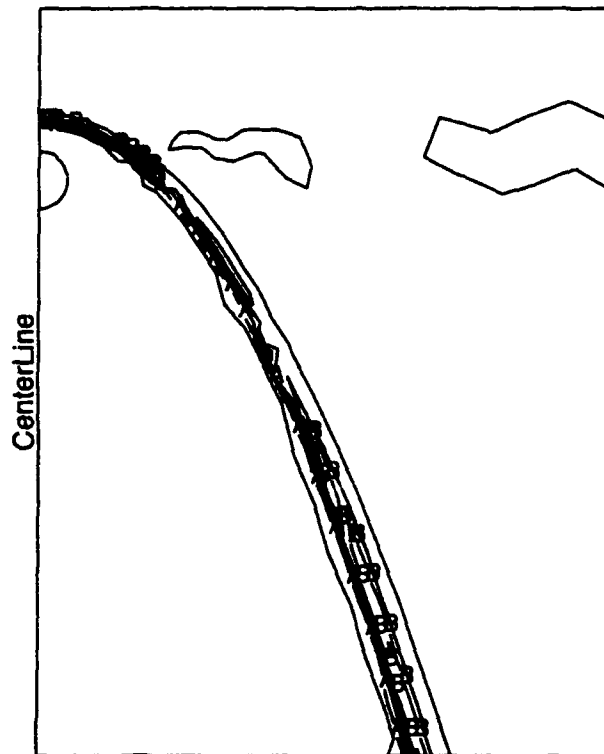


Figure 22(e). Ion densities for Mach 30.



Marked Levels

- A 0.50
- B 2.50
- C 4.50

Density

Figure 22(f). Ion densities for Mach 100.

5. SHEATH STRUCTURE ABOUT A SPHERICAL PROBE IN THE CHAOTIC LIMIT

5.1 Introduction

Several authors^{2,3} have recently shown that many electron trajectories in the vicinity of a positively charged sphere in a magnetic field exhibit chaotic behavior. This finding justifies the use of orbit-limited theory to calculate the contribution of such chaotic orbits to the electron density at a point. In the further approximation that the plasma is very cold, the charge density due to the chaotic orbits completely dominates the problem, since it is proportional to $T^{-1/2}$.

In this report, we calculate the space charge density and potential fields around a spherical probe with parameters appropriate to the TSS-1 subsatellite. We find that, for realistic temperature, potential, and magnetic field, the sheath becomes fully compacted at a density orders of magnitude below the density expected in flight.

5.2 Chaotic Orbits and Orbit-Limited Density

Among the characteristics of a chaotic orbit is that it completely fills the "magnetic bottle" to which it is restricted by its energy and angular momentum. Conversely, a point in phase space will be traversed exactly once by each chaotic orbit to which it is accessible. (If a point were traversed more than once by an orbit, the orbit would be periodic.) We can then use Liouville's theorem (that phase space density remains constant along an orbit) to calculate the space charge density at a point associated with the set of orbits assumed to be chaotic.

The first question to be addressed is what orbits are chaotic in the low temperature limit. We limit consideration to orbits having zero or slightly positive energies.

1. All orbits having canonical angular momenta within the Parker-Murphy limiting value are *not* chaotic. Their magnetic bottles have a finite intersection with the spherical probe, so that they will be collected before they can fill space. (It is possible to construct potentials such that not all magnetic bottles intersect the probe. We shall see that our final self-consistent potentials will not be pathological in that way.)
2. All orbits with sufficiently large angular momenta (i.e., large impact parameters) are insufficiently perturbed by the potential to be chaotic. For a long range potential (such as a coulomb potential) a temperature-dependent transition into this region must be formulated. We shall see that our self-consistent potentials drop off in such a way that no such formulation is needed.
3. We assume that all orbits with angular momenta beyond the Parker-Murphy limit, and within the range of the potential are chaotic or, rather, that the nonchaotic orbits within this range form a set of measure zero.

We express the density in terms of the parameters:

r	Radius (cylindrical)
ϕ	Potential
$\rho(r, \phi)$	Local charge density
ρ_0	Ambient charge density
T	Ambient plasma temperature (energy units)
B	Constant magnetic field (along z)
ω	eB/m
p_θ	Canonical angular momentum, $mr^2(\omega + \partial\theta/\partial t)$
U	$(p_r^2 + p_z^2)/2m$
P_1, P_2	Lower and upper bounds for chaotic orbits

The orbit-limited density is then given by⁴

$$\frac{\rho(r, \phi)}{\rho_0} = \frac{1}{\sqrt{2\pi m r^2 T^3}} \int_{P_1}^{P_2} dp_\theta \int_{\max(0, e\phi_{eff})}^{\infty} du \exp\left[\frac{e\phi_{eff} - U}{T}\right]$$

$$\phi_{\text{eff}} = e\phi \frac{(p_{\theta} - mr^2 \omega/2)^2}{2mr^2} .$$

The magnetic bottle for angular momentum p_{θ} is defined by $\theta_{\text{eff}} > 0$. Inside the magnetic bottle, the integral over kinetic energy, U , gives T . Outside the magnetic bottle the integral vanishes at low temperature as $\exp(e\phi_{\text{eff}}/T)$. Ignoring terms which vanish at low temperature, we have

$$\frac{\rho(r, \phi)}{\rho_0} = \frac{1}{\sqrt{2\pi m r^2 T^3}} (P_{\text{upper}} - P_{\text{lower}})$$

$$P_{\text{lower}} = \max \left\{ P_1, (mr^2 \omega/2) \left[1 - \sqrt{\frac{8e\phi}{m\omega^2 r^2}} \right] \right\}$$

$$P_{\text{upper}} = \min \left\{ P_2, (mr^2 \omega/2) \left[1 + \sqrt{\frac{8e\phi}{m\omega^2 r^2}} \right] \right\} .$$

5.3 Transformation to Dimensionless Units

It is convenient to work in units of the probe radius, a , and the magnetic energy unit $m\omega^2 a^2/8e$. Also, we replace the angular momentum variable with a dimensionless variable, w . The new variables are then:

Position	$(\sigma, \xi) = (r/a, z/a)$
Potential	$\psi = 8e\phi/m\omega^2 a^2$
Temperature	$\tau = 8e\theta/m\omega^2 a^2$

The equation for the local charge density becomes:

$$\rho(\sigma, \psi)/\rho_0 = \frac{1}{\sqrt{\pi\tau}} \sigma (w_{\text{upper}} - w_{\text{lower}})$$

where

$$w_{\text{lower}} = \max \left\{ \left(1 + \sqrt{\psi_0}\right) / \sigma^2, 1 - \sqrt{\psi} / \sigma \right\}$$

$$w_{\text{upper}} = \max \left\{ \left(1 + \sqrt{\psi_0}\right) / \sigma^2, 1 + \sqrt{\psi} / \sigma \right\}$$

and ψ_0 is the dimensionless potential on the probe.

In terms of the dimensionless variables and the density ratio, Poisson's equation becomes:

$$-\nabla^2 \psi = \frac{-Q_0 \rho(\sigma, \psi)}{\rho_0}$$

$$Q_0 = \frac{8e\rho_0}{m\omega^2 \epsilon_0} .$$

For the parameters of the TSS-1 subsatellite, the physical and dimensionless values are:

Table 2.

	Physical Value	Dimensionless Value
Probe radius	0.75 m	[unit distance]
Magnetic field	0.4 gauss	
Probe potential	5000 V	$\psi_0 = 252.8$
Plasma temperature	0.1 eV	$\tau = 5.06 \times 10^{-3}$
Plasma density	$1 \times 10^{12} \text{ m}^{-3}$	$Q_0 = 513.9$
Parker-Murphy radius	3.08 m	$\sigma_{\text{PM}} = 4.11$
Langmuir-Blodgett radius	3.64 m	$\sigma_{\text{LB}} = 4.85$

By comparing the Parker-Murphy (magnetic limiting) and Langmuir-Blodgett (space charge limiting) radii, we see that the two processes will be competitive in forming the sheath structure.

5.4 Computational Results

Calculations were done using a 2-dimensional (R-Z) finite element code with biquadratic quadrilateral elements. The computational grid (Figure 23) represents a sphere contained in a cylinder of radius 20-sphere radii and height 40-sphere radii, taking advantage of azimuthal and mirror symmetry. Self-consistent solutions to Poisson's equation (with space charge in the chaotic limit) were obtained for dimensionless ambient densities, Q_0 up to 0.69. Even at this density, three orders of magnitude below ionospheric parameters, the sheath edge occurs sufficiently close to σ_{PM} to make difficult solutions for further density increases.

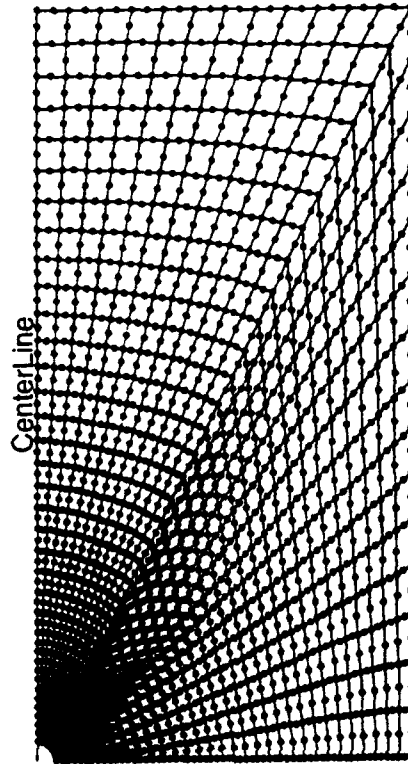


Figure 23. Computational grid of biquadratic elements, representing the region outside a sphere and within a cylinder of radius-20 sphere radii and height-40 sphere radii. Azimuthal and mirror symmetries are assumed.

Figure 24 shows electron density contours (ρ/ρ_0) when the potential satisfies Laplace's equation. The peak density is about 80 times ambient, and the "sheath radius" occurs at the computational boundary. Figures 25 – 28 show the potential and electron density contours for successively higher values of ambient density. With increasing ambient density, the sheath radius contracts toward the Parker-Murphy radius, and chaotic electron orbits are confined to the magnetic bottle for field lines between the Parker-Murphy radius and the sheath radius. Table 2 shows the sheath radius and the peak density ratio as a function

of ambient density. Because the total sheath charge can increase only slowly with increasing ambient density, the peak density ratio as well as the sheath volume decreases.

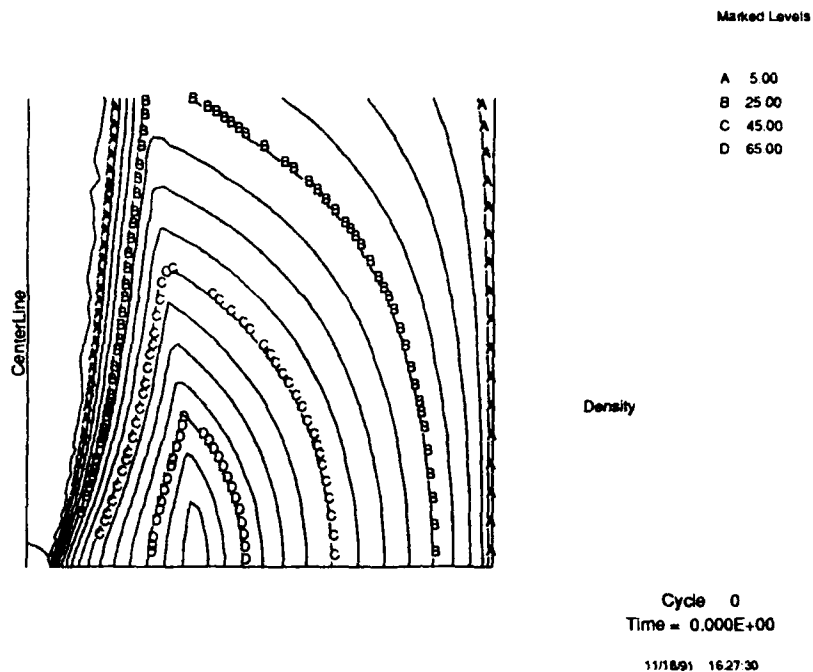
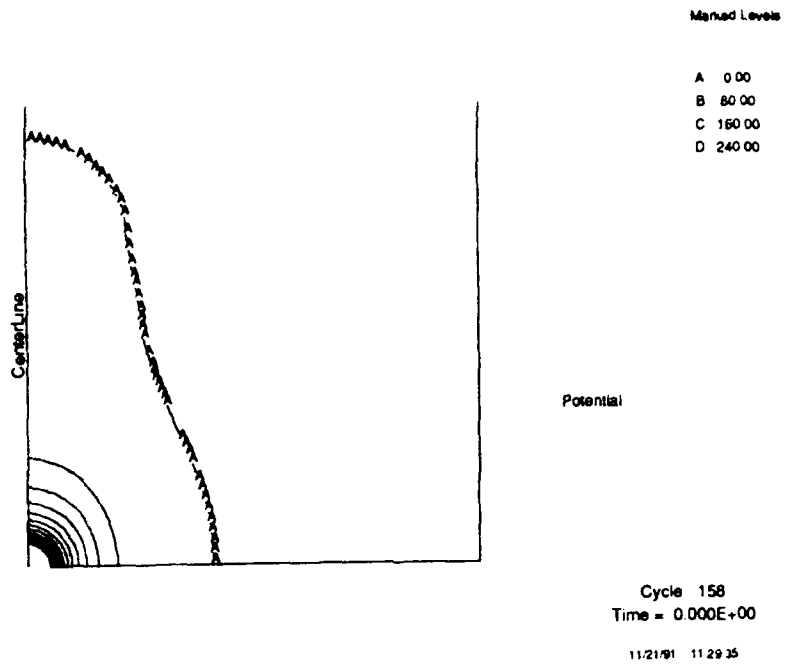


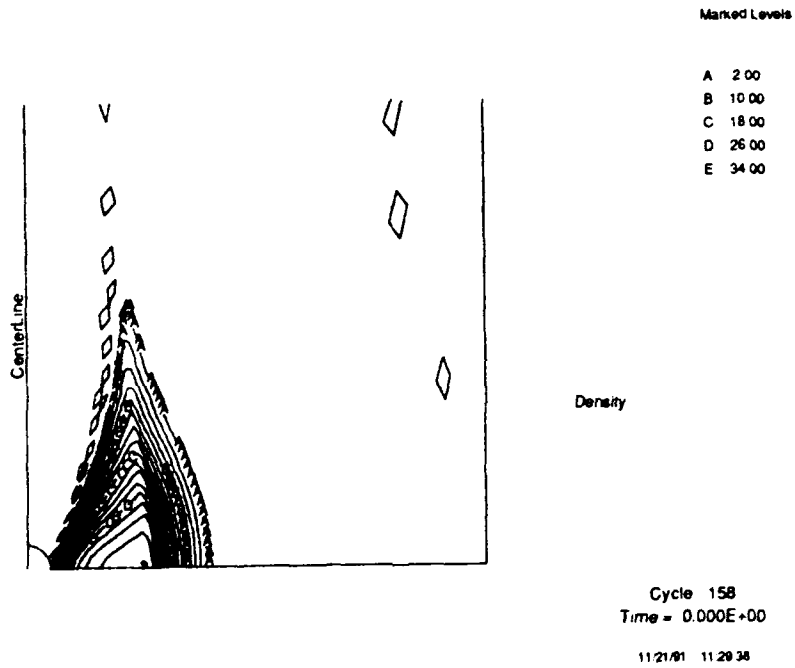
Figure 24. Electron density ratio contours calculated for potentials obeying Laplace's equation.

Table 3.

Density Q_0	Sheath Radius	Peak (ρ/ρ_0)
0.00	20	80
0.12	8.0	34
0.28	6.1	25
0.42	5.6	23
0.69	5.1	20

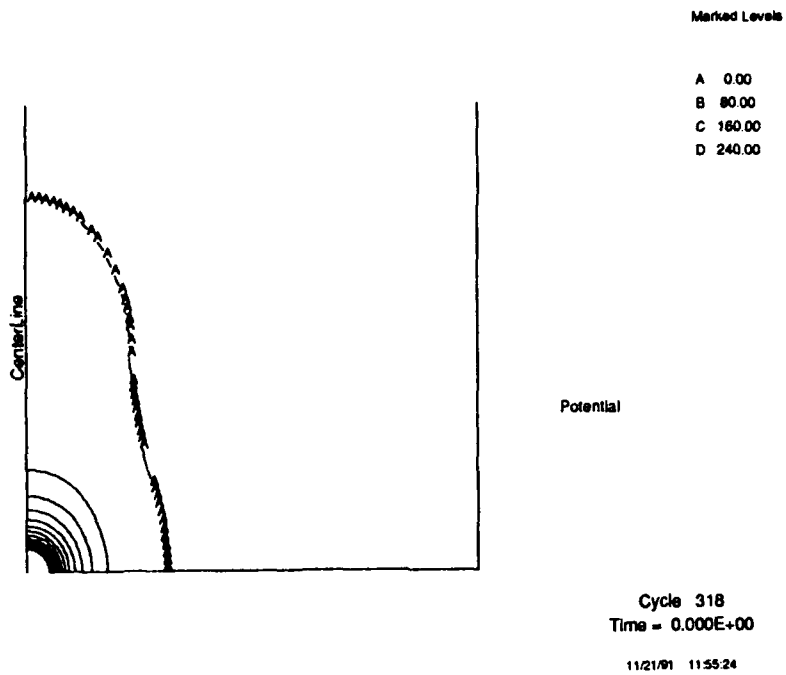


(a)

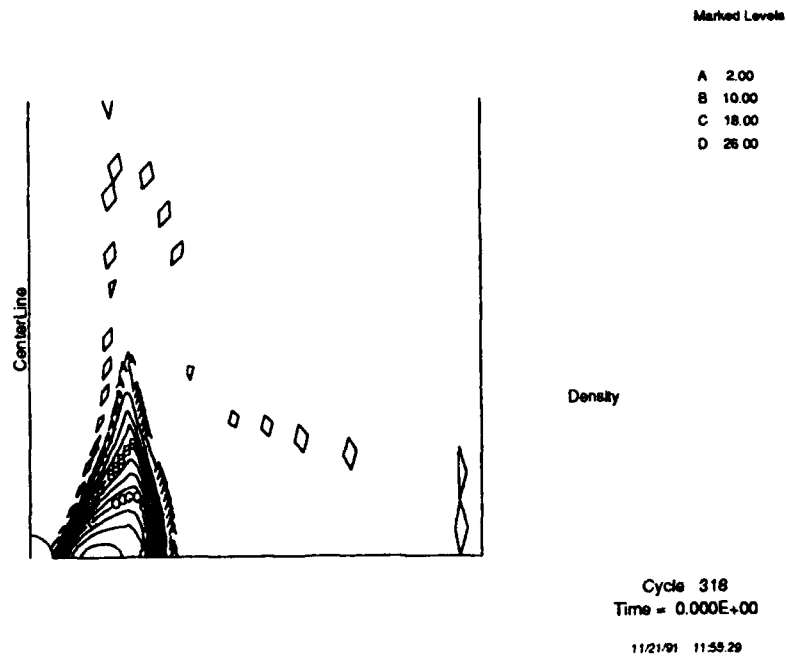


(b)

Figure 25. Potential contours (a) and electron ratio contours (b) for density $Q_0 = 0.12$.

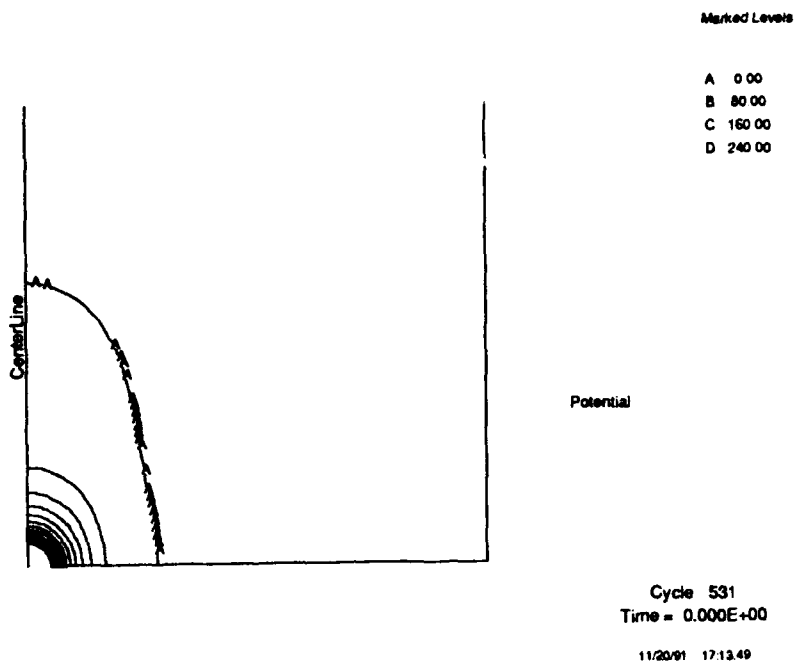


(a)

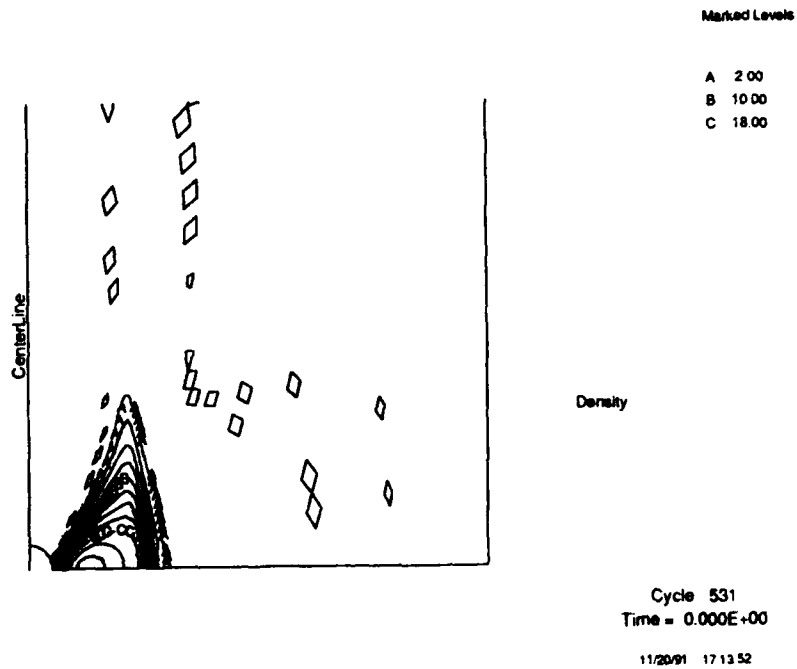


(b)

Figure 26. Potential contours (a) and electron density ratio contours (b) for density $Q_0 = 0.28$.

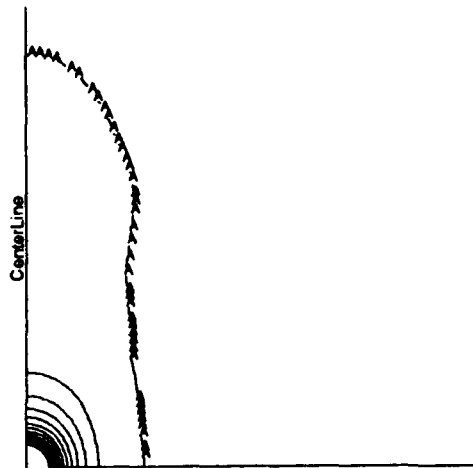


(a)



(b)

Figure 27. Potential contours (a) and electron density ratio contours (b) for density $Q_0 = 0.42$.



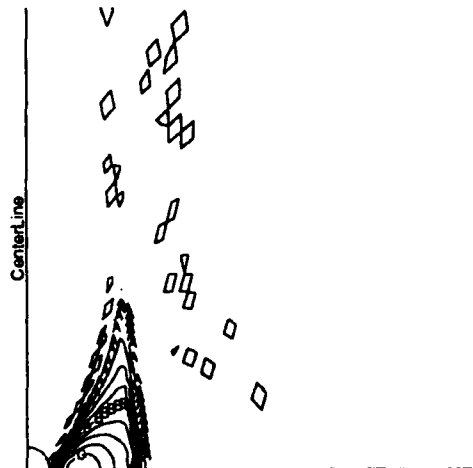
Marked Levels

- A 0.00
- B 80.00
- C 160.00
- D 240.00

Potential

Cycle 801
 Time = 0.000E+00
 11/21/91 16:37:51

(a)



Marked Levels

- A 2.00
- B 10.00
- C 18.00

Density

Cycle 801
 Time = 0.000E+00
 11/21/91 16:37:54

(b)

Figure 28. Potential contours (a) and electron density ratio contours (b) for density $Q_0 = 0.69$.

Figure 29 shows the inner and outer radii of magnetic field lines that contribute electron density to points on the symmetry plane. The equilibrium potential structure is such that both the upper and lower bounds are monotonic functions of radius, so that points within the sheath are forbidden to electrons from field lines that do not pass through the sheath. This means that the calculation is insensitive to a precise criterion for the sheath condition.

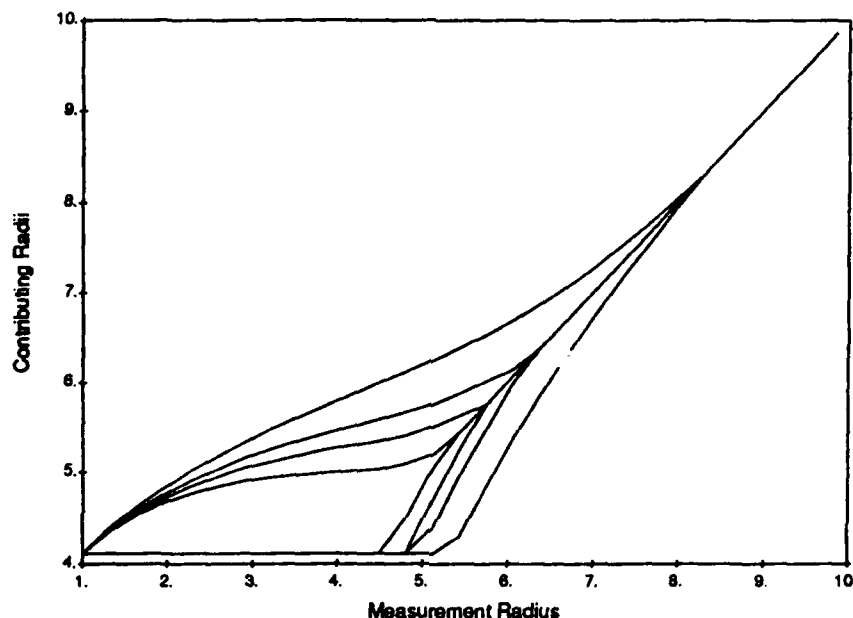


Figure 29. Radii of magnetic field lines contributing to densities at various radii on the symmetry plane. Outermost envelope, $Q_0 = 0.12$; second envelope, $Q_0 = 0.28$; third envelope, $Q_0 = 0.42$; innermost envelope, $Q_0 = 0.69$.

5.5 Conclusions

We have calculated the sheath structure for a magnetic probe under the assumption that all orbits which enter the sheath and cannot be collected are chaotic. For the parameters considered, the sheath dimension normal to the magnetic field approaches the Parker-Murphy radius at rather low ambient density. A region of high electron density fills the magnetic bottle for electrons entering the sheath between the Parker-Murphy radius and the sheath radius.

As the density increases further, the contribution of collected electrons and the presence of ambient ions will modify the sheath structure.

6. THREE-DIMENSIONAL MAGNETIC SHEATH CALCULATIONS

We used the DynaPAC computer code to perform 3-dimensional calculations of a 0.8 m radius, 1000 V sphere moving through a plasma with a magnetic field. The orbital motion was taken as 7500 m/sec in the x direction, and the magnetic field was 0.4 gauss in the y direction. The plasma density was 10^{12} m^{-3} , and the plasma temperature was 0.1 eV. The ion species was taken to be O^+ .

Figure 30 shows the wake of the uncharged object. The calculation uses a shadowing algorithm to obtain the "neutral approximation" results, then applies an electric field correction.

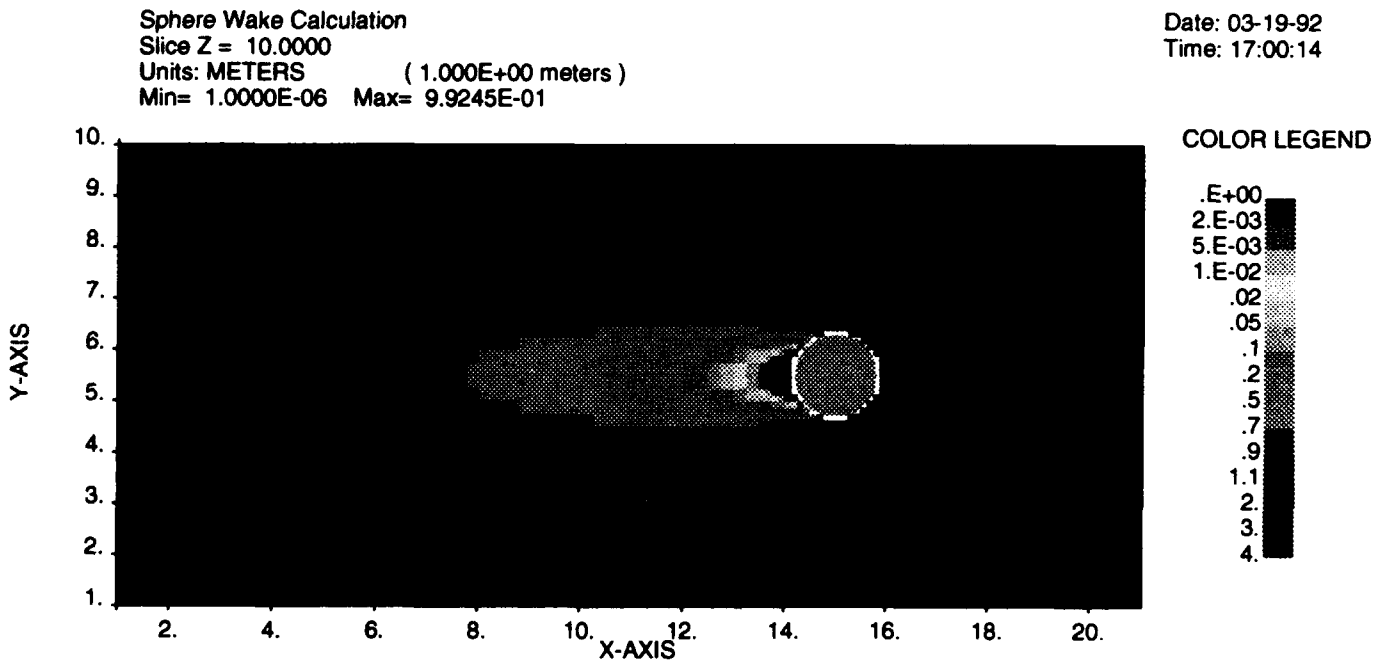


Figure 30. Plasma wake densities for an uncharged, 0.8 m radius sphere.

Figure 31 shows the electrostatic potential calculated using the object-wake ion densities. The calculation takes account of reduced screening due to low ion density in the wake as well as reduced wake-side electron currents. Thus, the high positive potential extends into the wake.

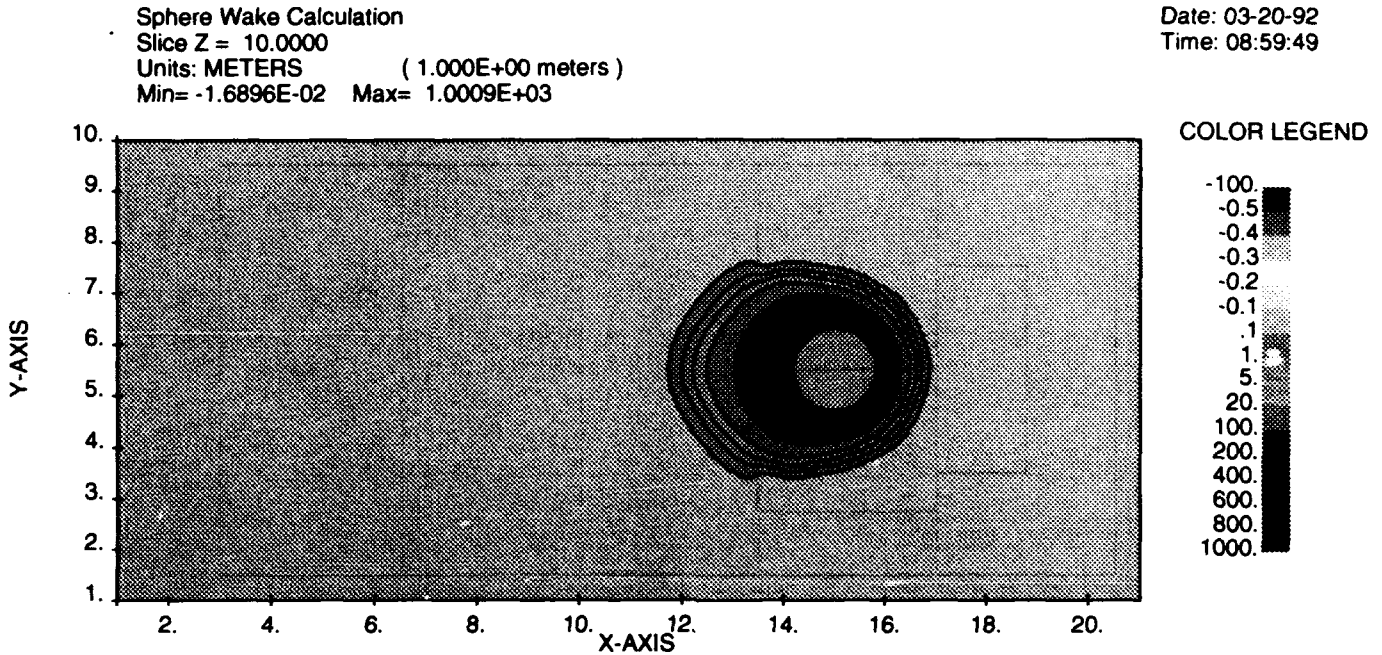


Figure 31. Electrostatic potentials calculated with the sphere at 1000 volts and the ion densities of Figure 30.

It is apparent from Figure 31 that the initial wake calculation is wrong. The wake of a positive object is formed not by the object surface, but by the much larger ion stagnation surface. The ion stagnation surface coincides with the 5 V contour level in the ram direction and drops to lower potential values on the sides of the sheath since the electric field is oblique to the ram velocity. Figure 32 shows wake ion densities calculated as in Figure 30 but now using the ion stagnation surface as the shadowing surface.

Sphere Wake Calculation
Slice Z = 10.0000
Units: METERS (1.000E+00 meters)
Min= 0.0000E+00 Max= 3.9240E+00

Date: 03-23-92
Time: 09:53:26

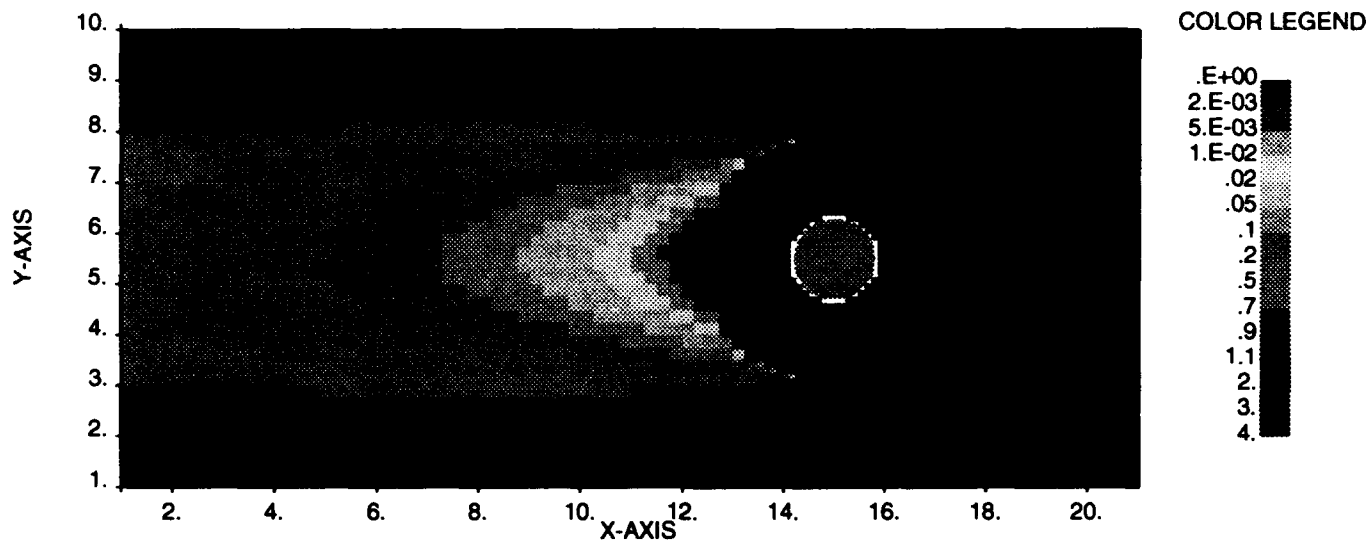


Figure 32. Ion densities calculated using the ion stagnation surface as a shadowing surface.

Figure 33 shows potentials calculated using the wake ion densities of Figure 32. Also, the calculation uses a new space-charge formulation that allows the wake region to be electron rich. We see the positive potentials extending further into the wake, and negative potentials down to about a half volt negative.

Sphere Wake Calculation
 Slice Z = 10.0000
 Units: METERS (1.000E+00 meters)
 Min= -3.9942E-01 Max= 1.0008E+03

Date: 03-20-92
 Time: 15:29:41

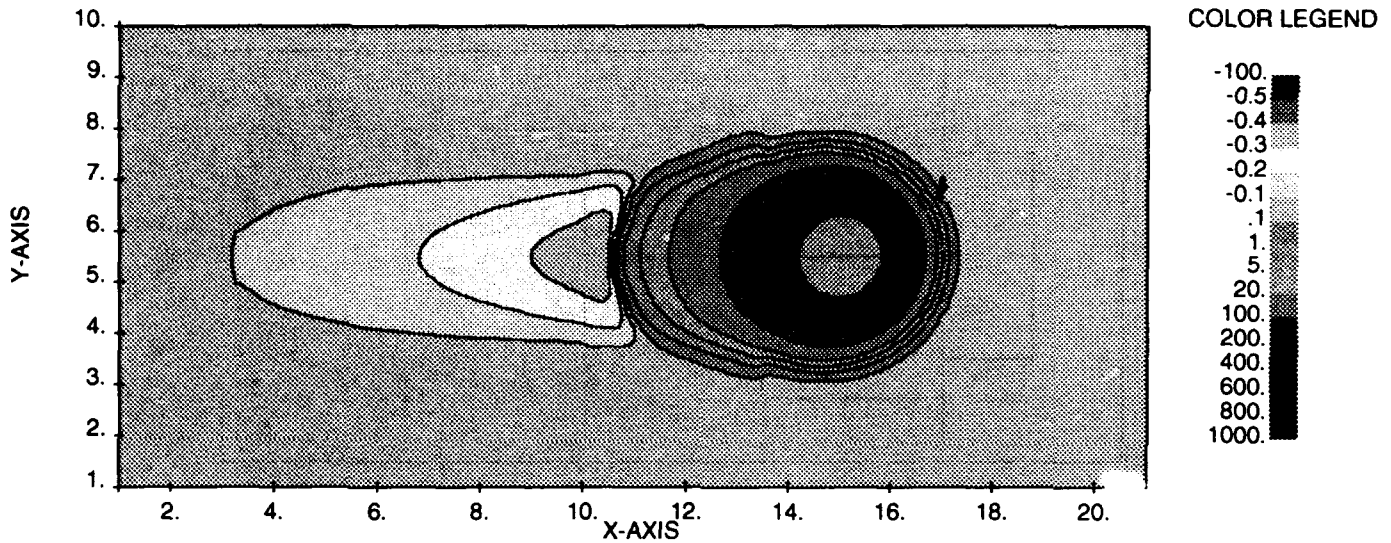


Figure 33. Electrostatic potentials calculated using ion densities similar to Figure 32, and a space charge formulation allowing the wake to be electron rich.

Finally, we add a magnetic field along the Y axis. To determine self-consistent potentials in a magnetic field requires generating electrons at a "sheath surface" and tracking them to determine self-consistent electron densities within the sheath. Figures 34(abc) show the resultant electron densities, and Figures 35(abc) show the potentials. The three electron density plots show low electron densities near the $\pm Y$ sides of the sphere but relatively higher densities in the other directions. This indicates that a belt of electrons is now orbiting the sphere in the X-Z plane. This belt of electrons has little effect on the ram side (where its charge is neutralized by the ions), but on the wake side (where there were previously no ions or electrons) it squeezes the sheath boundary close to the object, as is seen by comparing Figures 35(abc) with Figure 33. It also reduces the Z sheath dimension relative to the Y sheath dimension, although for these parameters the asymmetry only becomes apparent wakeward of the sphere. (Rough calculations for other parameters show far more apparent asymmetry.)

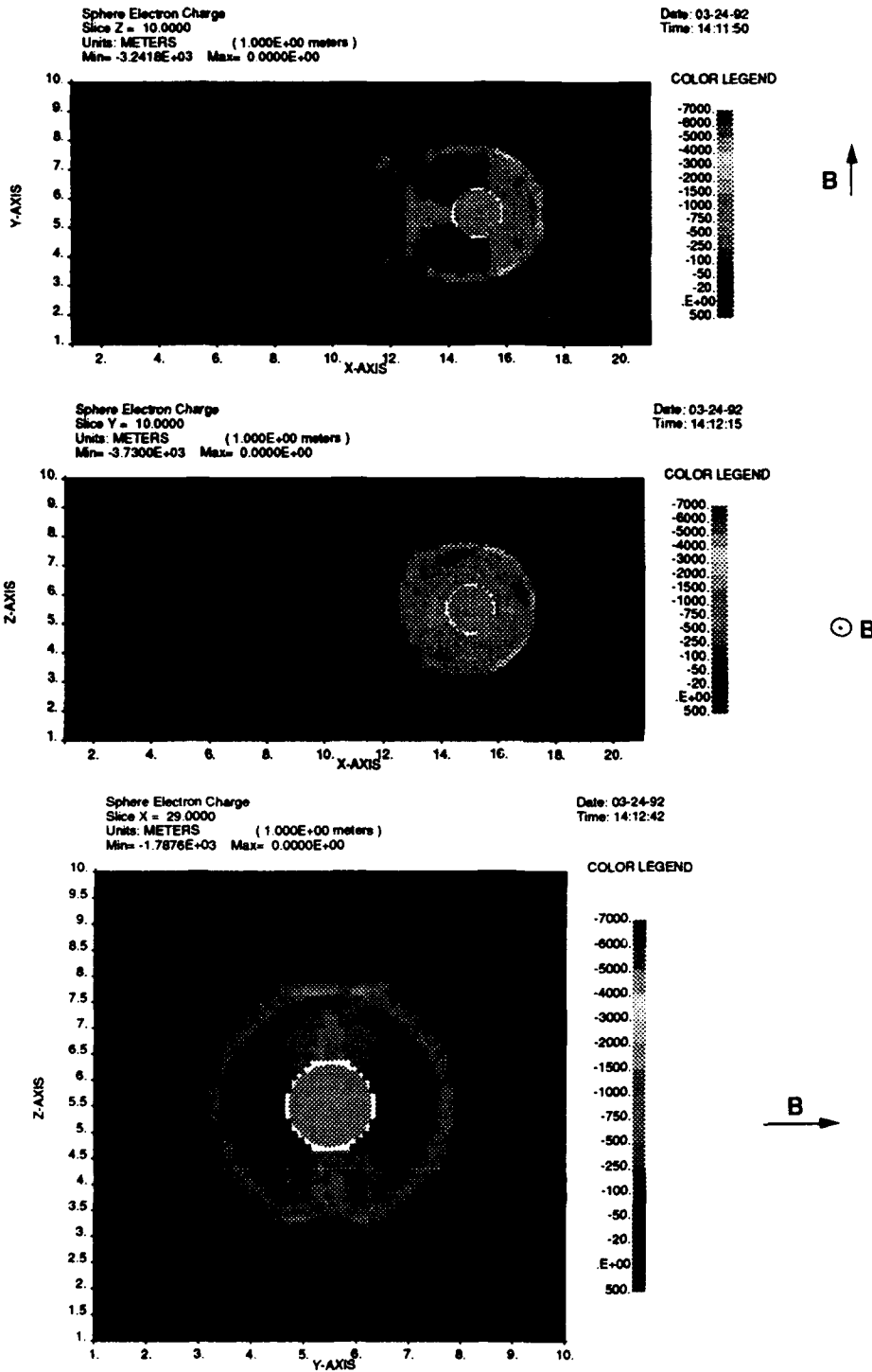


Figure 34. Tracked electron densities in the sheath region, with a magnetic field of 0.4 gauss in the y direction: (a) X-Y plane; (b) X-Z plane; (c) Y-Z plane.

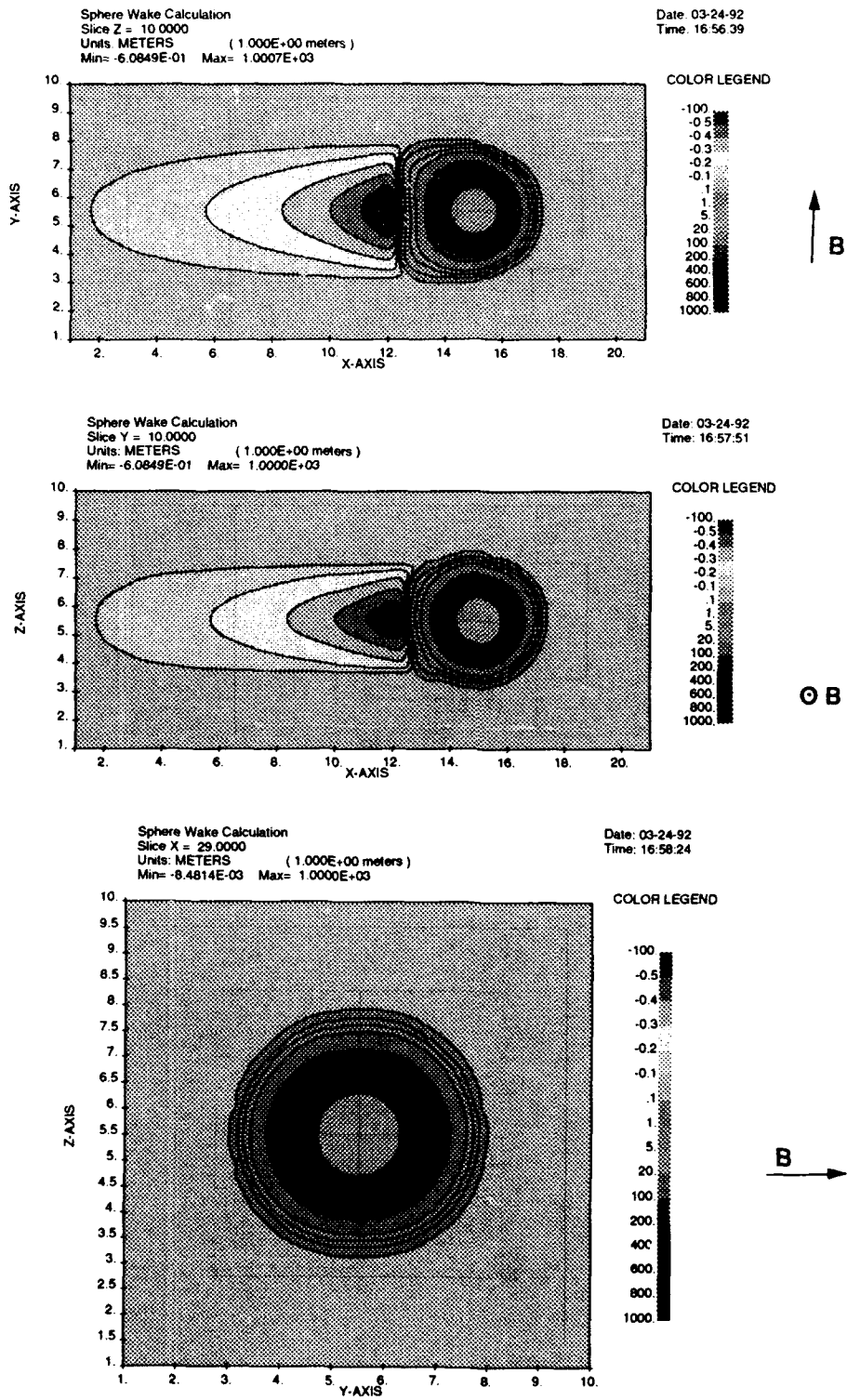


Figure 35. Electrostatic potentials calculated using the tracked electron densities in the sheath region: (a) X-Y plane; (b) X-Z plane; (c) Y-Z plane.

7. ANALYSIS OF HIGH RESISTANCE PAINT ON THE TSS-1 SUBSATELLITE SHEATH

The laboratory results of Lebreton, recently corroborated by Carruth and Vaughn, indicate that the paint on the TSS-1 subsatellite is not a conductor for the plasma conditions anticipated during flight. In this brief note, we present calculations and analysis of the asymmetric electron collecting sheath for the subsatellite as presently configured, that is with a conducting belly band, conducting screw heads, and including snapover on the paint. We compare the sheath structure with that calculated for a perfectly conducting sphere. For high applied potentials, the conducting belly band is shown to cause a sheath about 50% of that for a conducting sphere. The analysis assumes that secondary electrons from the paint are collected by the exposed conductors (snapover of the paint); essentially, none of the current is collected through the paint. Numerical calculations of the 3-dimensional sheath show that at 1000 V the average satellite surface potential is 500 V and the sphere collects about two-thirds the current of a conducting sphere.

Two modifications to the subsatellite that increase sheath symmetry and collected currents are under consideration. The first is to cover the paint with an indium tin oxide (ITO) layer. The second is to expose additional conducting strips on the subsatellite surface and use secondary electron transport to equilibrate surface potentials. Both modifications to the subsatellite are analyzed and test parameters are suggested to verify the efficacy of the proposed solutions. Tests must be performed at the appropriate plasma current density and exposed conductor geometry if we are to be certain that TSS-1 will accomplish its scientific objectives.

7.1 Analysis and Calculations of the Present SubsateLLite Configuration

In its present configuration, the TSS-1 subsatellite has an exposed conducting belly band as well as numerous exposed conducting screw heads. We have

performed a simplified analysis of the size and symmetry of the potential field surrounding an isolated conducting ring with the dimensions of the belly band. The analysis predicts that an isolated ring would have the about 60% the charge of a perfectly conducting sphere; the sheath potentials would have asymmetries greater than a factor of two. Numerical calculations of the 3-dimensional electron-collecting sheath support the analytical results. The conclusion is that only small modifications may be required to substantially symmetrize the subsatellite sheath potentials.

7.1.1 Analysis of the Sheath Potentials Surrounding the Belly Band

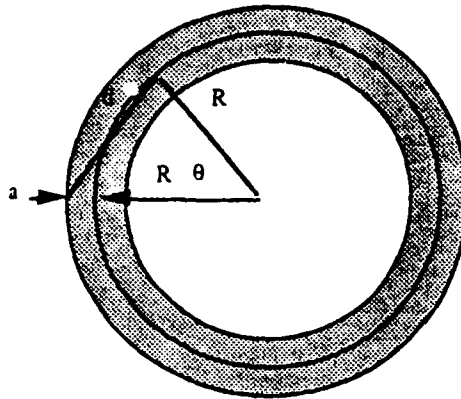
Previously, we have documented how secondary electron transport reduces the effect of insulating surfaces on the potentials near conductors biased positive with respect to a surrounding plasma.⁵ If we ignore the insulating surfaces completely, we can calculate the capacitance of a conducting ring the dimensions of the belly band. With this approximation, we estimate the total sheath charge is about 60% of a conducting sphere. The sheath asymmetry, estimated by comparing potentials the conducting ring produces at the poles of the satellite, is greater than a factor of two.

Assume the belly band is a circle of radius R formed out of conducting wire of radius a. If $R \gg a$, we can assume that all of the charge is contained in a line of charge in the middle of the wire. The potential on the outer surface of the wire is obtained by integrating the line charge using the free space Green's function,

$$\phi_{ring} = \frac{1}{4\pi\epsilon_0} \int_{-\pi}^{\pi} \frac{\pi d\theta}{\sqrt{(a+R)^2 + R^2 - 2(a+R)R\cos\theta}}$$

where the total charge on the ring is

$$Q_{ring} = \int_{-\pi}^{\pi} \pi R d\theta = 2\pi R \tau .$$



The potential on the outer edge of the belly band is calculated using the law of cosines.

The total ring charge is linearly dependent upon the major radius, R , and only logarithmically on the ratio of a to R . The capacitance of the conducting ring is

$$C_{\text{ring}} = \frac{Q_{\text{ring}}}{\Phi_{\text{ring}}} = \frac{2\pi R\tau}{4\pi\epsilon_0 \int_{-\pi}^{\pi} \frac{\tau d\theta}{\sqrt{(a+R)^2 + R^2 - 2(a+R)R\cos\theta}}}$$

It is useful to discuss the ring capacitance in terms of an effective radius,

$$C_{\text{ring}} = 4\pi\epsilon_0 R_{\text{eff}}$$

where

$$R_{\text{eff}} = R \times \left(\frac{\pi}{\int_0^{\pi} \frac{d\theta}{\sqrt{(a/R+1)^2 + 1 - 2(a/R+1)\cos\theta}}} \right)$$

$$= Rf(a/R) .$$

The subsatellite has a radius of 0.8 meters. We estimate the belly band radius is somewhere between 2 cm and 5 cm. The ratio function, $f(a/R)$, varies between 0.55 and 0.67 for this range of radii. Thus the ring has between one-half and two-thirds the capacitance of an ideal conducting sphere. The potential asymmetry is larger, however, because the distance from the ring to the poles is $\sqrt{2} R$.

$$2.1 \leq \frac{\Phi_{\text{ring}}}{\Phi_{\text{pole}}} \leq 2.6 .$$

These analytical results should be tested on a small laboratory sphere completely covered with Goddard white paint, except for an exposed equatorial, conducting ring. The sphere should be biased to potentials above 300 V and exposed to a ionosphere-like plasma. If the results agree with this analysis, they indicate that, although the paint will impair the sheath symmetry, substantial electron currents will be collected by the present subsatellite configuration.

Three-dimensional computer calculations were performed to examine numerically the sheath asymmetries and reduced electron collection caused by the poor conductivity of the white paint on the subsatellite surface. In order to perform the calculations in the limited time available, the following assumptions were made:

1. The only significant exposed conductors were a 10 cm wide belly band and the cells of screw heads at the edges of the eight panels. Total exposed conducting area is just under 12%.
2. Both motion and magnetic effects on the sheath were ignored (as opposed to the calculations we presented at the May IWG).

The calculations were run using the NASCAP/LEO code, which solves Poisson's equation using analytical formulations of space charge and surface secondary electron transport.⁶ Plasma conditions chosen were $n_e = n_i = 10^{12} \text{ m}^{-3}$, $T_e = 0.1 \text{ eV}$, typical of the daytime ionosphere expected during the TSS-1 mission. The calculations were performed for satellite

potentials of 200 V and 1000 V. The 200 V results overestimate the degree of snapover on the subsatellite surface; potentials on the surface varied between the applied potentials and 0 volts. The 1000 V case showed a minimum surface potential of 300 V. The attached figures are for the 1000 V case and show the satellite model where the gold and aluminum surfaces were conducting, the calculated distribution of surface potentials including snapover, and a cross section through the sheath showing the degree of asymmetry of the calculated sheath. The calculated space-charge-limited current (ignoring motion and magnetic field effects) is 0.38 amperes compared with .56 amperes calculated using NASCAP/LEO for the same sphere entirely at 1000 V. Analytical Langmuir-Blodgett predicts 0.5 amperes for the same thermal electron current density. The NASCAP/LEO calculations are representative. Laboratory testing and more detailed calculations are required in order to determine the actual current collection by the TSS-1 subsatellite as presently configured.

7.1.2 Analysis of ITO Coating on the Satellite

Ideally, the surface of the subsatellite should be perfectly conducting. It has been proposed to cover the existing, poorly conducting surface with an ITO layer, which would conduct the electron current to the aluminum skin through a series of grooves cut into the white paint. ITO has been used on high altitude spacecraft to control surface charging. Typical deposition thickness is a few hundred angstroms with measured surface resistivity of 5 K ohms on a 30 cm x 30 cm FEP teflon sample. Higher conductivity is observed over glass substrates, but the FEP results are probably representative of what can be expected on the large area TSS-1 panels. If the distance between grooves in the paint were 10 cm, then the resistance would also be the order of 5 K ohms. The peak expected electron currents, including sheath focusing, are of order 10^{-5} amps/cm², the current to a 10 cm x 10 cm square is 10^{-3} amps. This corresponds to only a few volt potential drop, better than necessary for TSS-1.

Several issues concerning the ITO coating must to be resolved before the satellite is modified.

1. Does the ITO resistance increase after exposure to vacuum as does the existing white paint. Bear in mind that both are metal oxides (the paint is

ZnO), and it is the thinness of the ITO that makes it appear transparent. The ITO layers are typically 1/10,000 of the present paint thickness.

2. Will the ITO layer be damaged due to local heating. For the example cell size, the heating at 1000 V is the order of a watt for 10^{-4} cm³. Testing must be performed, after days of outgassing, at the highest expected current levels.
3. Is the ITO layer mechanically robust enough to maintain electrical continuity after launch and deployment.

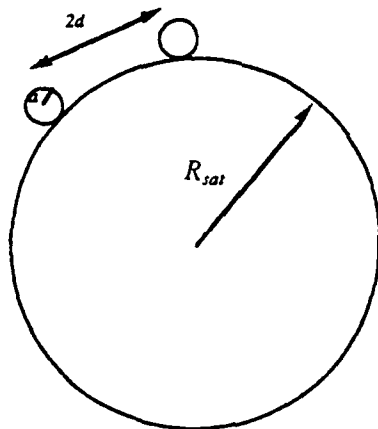
Bear in mind that ITO coatings were developed for the same nano-ampere per square centimeter, geosynchronous charging, currents as the present, inadequate paint. It is also disturbingly close in chemical formulation. ITO over the paint must be tested thoroughly at extreme flight current levels.

7.1.3 Electron Collection by Surface Snapover

An alternative approach to enhancing the TSS-1 current collection is to take advantage of the fact that ZnO has a high secondary electron yield ($Y_{\max} \approx 6.0$) and that secondary electrons can transport incident electron fluxes to exposed conductors. For metal oxides, incident electrons with energies between ~60 eV and ~5000 eV emit more than one secondary electron per incident electron. Electric fields parallel to the surface accelerate the secondary electrons toward exposed conductors. There exists a stable potential distribution such that for each incident electron, a secondary electron is collected by a nearby exposed conductor. This phenomenon has been studied extensively in conjunction with electron collection by high voltage solar arrays, where it enhances electron current collection by spreading interconnect potentials on to coverslips. It has been observed both in the laboratory and in LEO by the PIX-II solar array flight experiment.⁷ For TSS-1, snapover is exactly the desired effect—spread the subsatellite chassis potential onto the surface of the paint and collect the plasma current from the paint surface by secondary electron transport. The effectiveness of this process can be tested on small samples in the laboratory by covering them with either a grid of wires or scoring a grid pattern through the paint. Scoring requires that the grooves be wide compared with the thickness of

the paint; other than that, the surface potentials are very insensitive to the groove width. Thus, an increase of only a few percent of exposed conductor would be required. The theory shows that the number of grid lines per object is the driving parameter, not the absolute spacing of the grid. As with the ITO, extensive testing at high current densities and applied voltages is mandatory. In this section, we present a simple theory of how to scale results from small samples to TSS-1, a discussion of the uniformity of the resultant sheath .

We have developed a very simple theory of how the surface potential distribution depends on sphere size, wire (or groove) separation, and wire (or groove) radius. Let the subsatellite be a large sphere of radius R_{sat} , covered with wires of radius a , separated by spacing $2d$.



Assume $R_{sat} \gg d \gg a$. If the satellite had been a perfectly conducting sphere of potential ϕ_{sat} , the mean electric field over the surface would be

$$(E) \approx \frac{\phi_{sat}}{R_{sat}}$$

If only the wire conductors (or exposed conductors) have significant charge, then they would have a surface field enhanced by the inverse of the fractional area of exposed conductor,

$$E_{cond} \approx \frac{d\phi_{sat}}{aR_{sat}}$$

The potential drop at the midpoint between conducting wires is approximately

$$\phi_{\text{con}} - \phi_{\text{mid}} = \Delta\phi \approx \frac{\phi d}{R_{\text{sat}}} \ln\left(\frac{d}{a}\right).$$

Note that the diameter of the wire (or groove) enters only logarithmically. Thus a mesh of very thin wires acts as an equipotential surface but can be almost 100% transparent. Vacuum tube designers have known this for almost a century. For TSS-1, the fractional area of exposed conductor need not be large for snapover to occur; the length of groove needs to be long compared with spacing, or else they have to be in a grid pattern.

For TSS-1, if we want snapover by 200 V, we want the midpoint to be at potential greater than the first crossover of the secondary yield curve, i.e., around 50 V. For example, at an applied 200 V potential, all surface potentials would be greater than 140 V for the following parameters.

$$\begin{aligned} a &= 0.5 \times 10^{-3} \text{ m} \\ d &= 5 \times 10^{-2} \text{ m} \\ R_{\text{sat}} &= 0.8 \text{ m} \\ \Delta\phi &\approx \frac{200 \times 5 \times 10^{-2}}{0.8} \ln\left(\frac{5 \times 10^{-2}}{0.5 \times 10^{-3}}\right) \\ \Delta\phi &\approx 57 \text{ V} \end{aligned}$$

This suggests that the sphere would have snapped over by 200 volts. Again, the snapover potential depends on there being more than one conductor whose length is long compared with spacing (or else the logarithmic dependence goes over to a stronger function of wire thickness), and the spacing must be small relative to the object radius.

The potential field appears very uniform just a short distance from the surface. We can write the potential above a planar array of wires as

$$\phi(x, y) = \langle \phi_{\text{surface}} \rangle + \sum A_n \cos\left(\frac{2\pi n x}{2d}\right) \exp\left(-\frac{2\pi n y}{2d}\right)$$

where the first term is the average field, and the second term represents the variation along the surface in the x direction and how the variation dies off exponentially above the surface, in the y direction. This potential satisfies Laplace's equation. The term which extends the farthest above the surface is the first harmonic in $2d$, the wire spacing. Even this term is down by two orders of magnitude at a distance equal to the wire spacing above the surface. That is only 10 cm from the surface for the example above. Again, designers of gridded vacuum tubes have known and used this phenomenon for most of this century.

7.2 Conclusions

The present paint and geometry of exposed conductors will lead to a TSS-1 sheath reduced by almost half, with over a factor of two asymmetry. Two possible approaches to increase the subsatellite electron collection and sheath symmetry have been analyzed. Neither should be implemented without substantial laboratory tests at TSS-1 current density levels (0.1 amps/m²), TSS-1 potentials (1000 – 3000 V) and TSS-1 vacuum duration (heat and vacuum for 3 days). Application of ITO is the simplest conceptually, but it may be risky because ITO has not been tested at LEO current electron current densities or for large areas applied over painted surfaces after long duration to space conditions. Taking advantage of surface snapover requires laboratory confirmation that exposed conductors will indeed spread the subsatellite potential onto the surface of the paint.

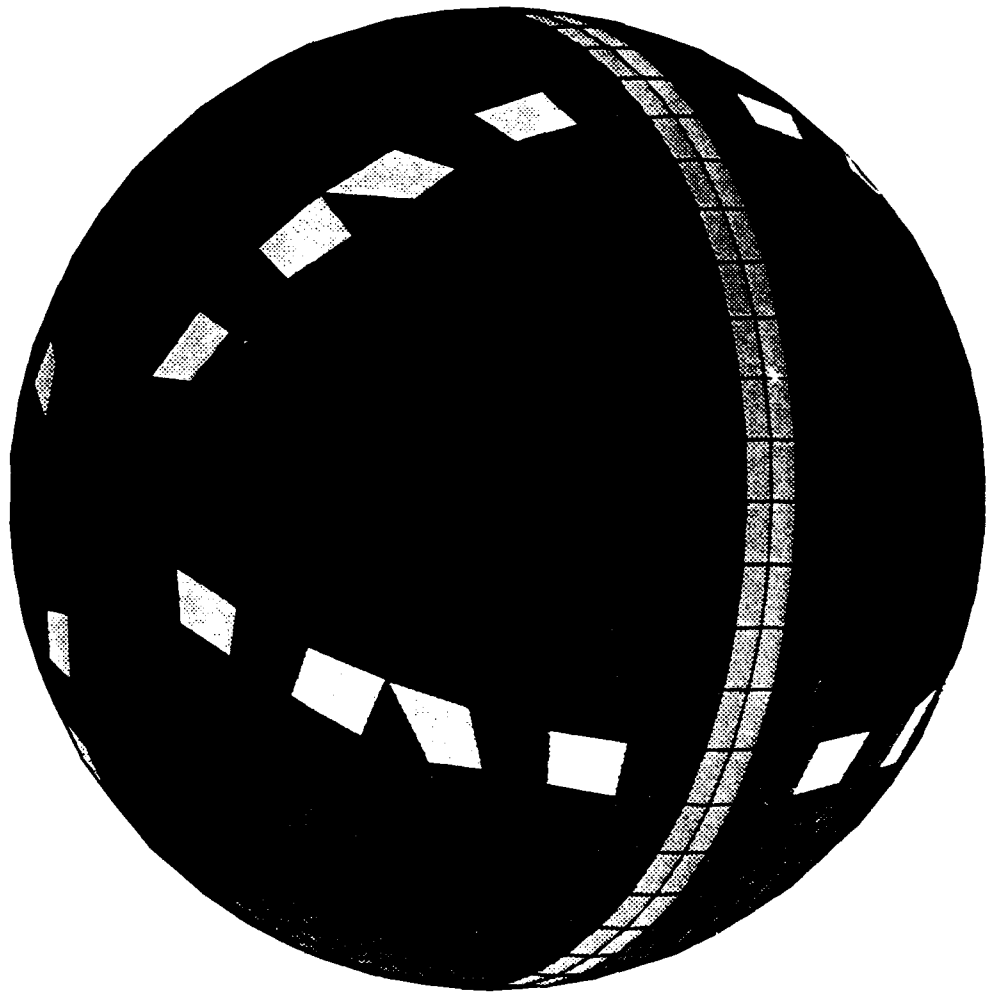
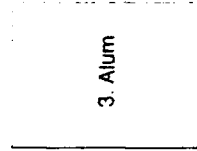
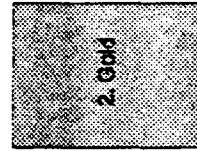
Acknowledgments

Special thanks to Marilyn Oberhardt and Dave Hardy for suggesting the calculations and insisting that they be written up, to Ralph Carruth and Jason Vaughn for keeping us informed of their lab results, and Dale Ferguson for providing data on ITO.

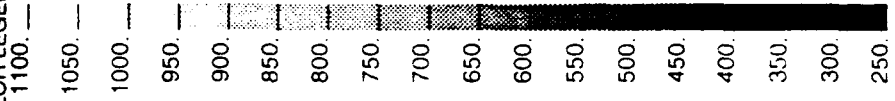
REFERENCES

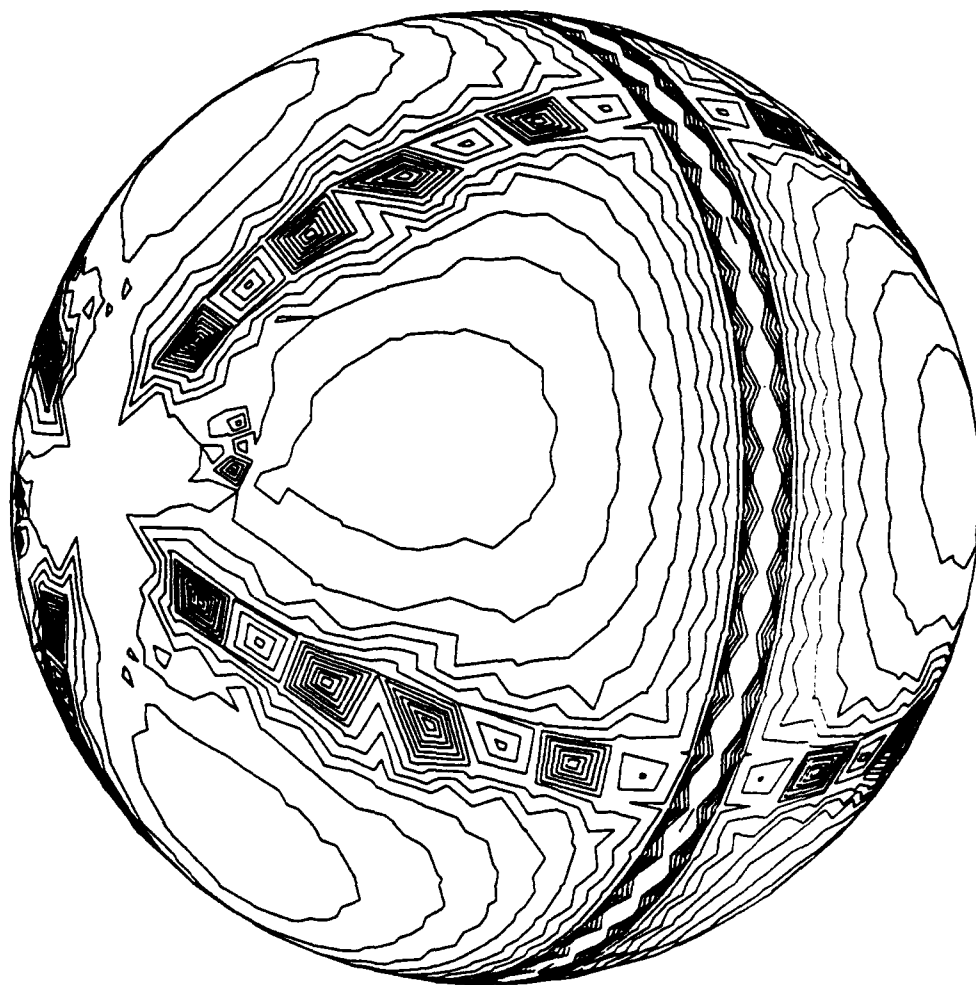
1. Goldstein, H., *Classical Mechanics*, Addison-Wesley, 1950.
2. Kunhardt, E. E., unpublished, 1990.
3. Sonmor and Laframboise, *Geophysics Research Letters*, 18, 1619, 1981.
4. Mandell, M. J., Rotenberg, M. R. and Katz, I., AFGL-TR-87-0331, ADA237672.
5. Katz, I. and Mandell, M. J., "Differential Charging of High-Voltage Spacecraft: The Equilibrium Potential of Insulated Surface," *Journal of Geophysical Research*, 87, 4533, 1982.
6. Mandell, M. J., Katz, I. and Cooke, D. L., "Potentials on Large Spacecraft in LEO," *IEEE Transactions on Nuclear Science*, 29, 1584, 1982.
7. Grier, N. T., "Plasma Interactions Experiment II: Laboratory and Flight Results," Spacecraft Environment Interactions Technology Conference, Colorado Springs, CO, Oct. 4-6, 1983, NASA CP-2359, 33, 1985.

COLOR LEGEND

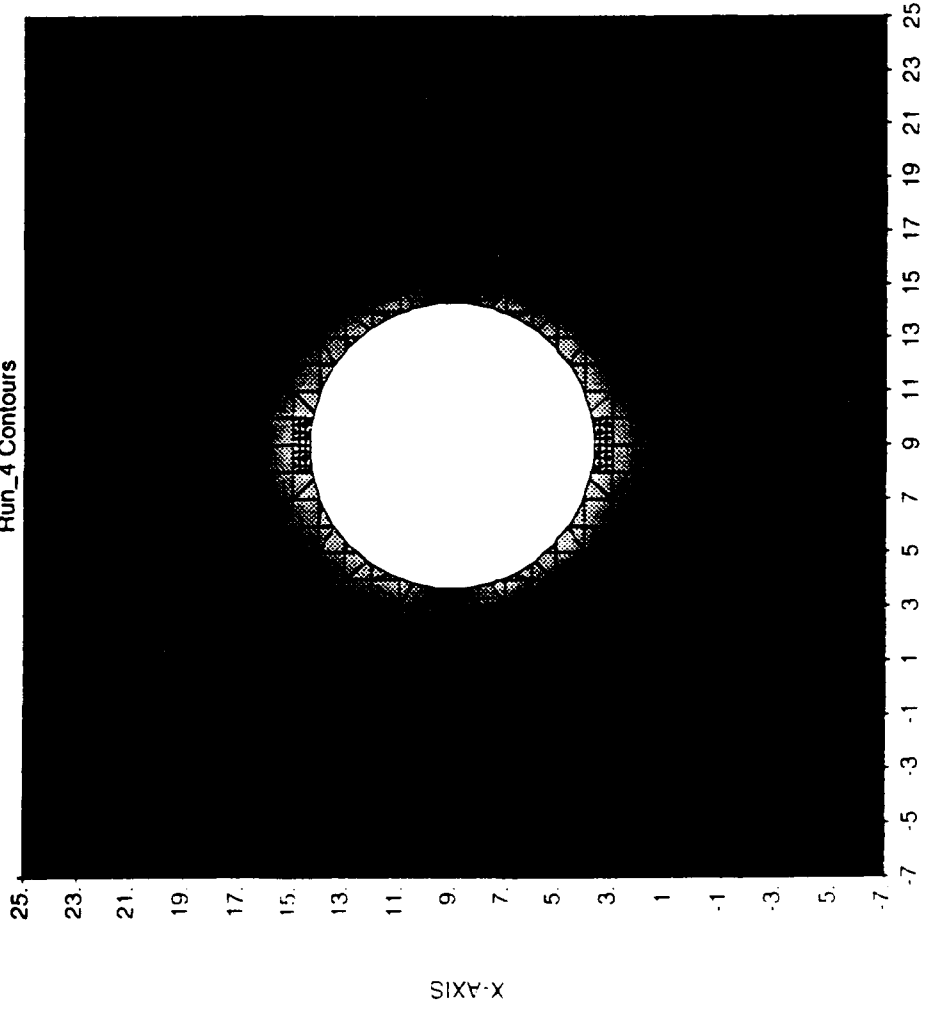


COLOR LEGEND

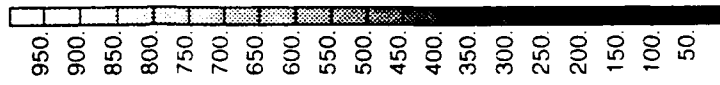




Run_4 Contours



COLOR LEGEND

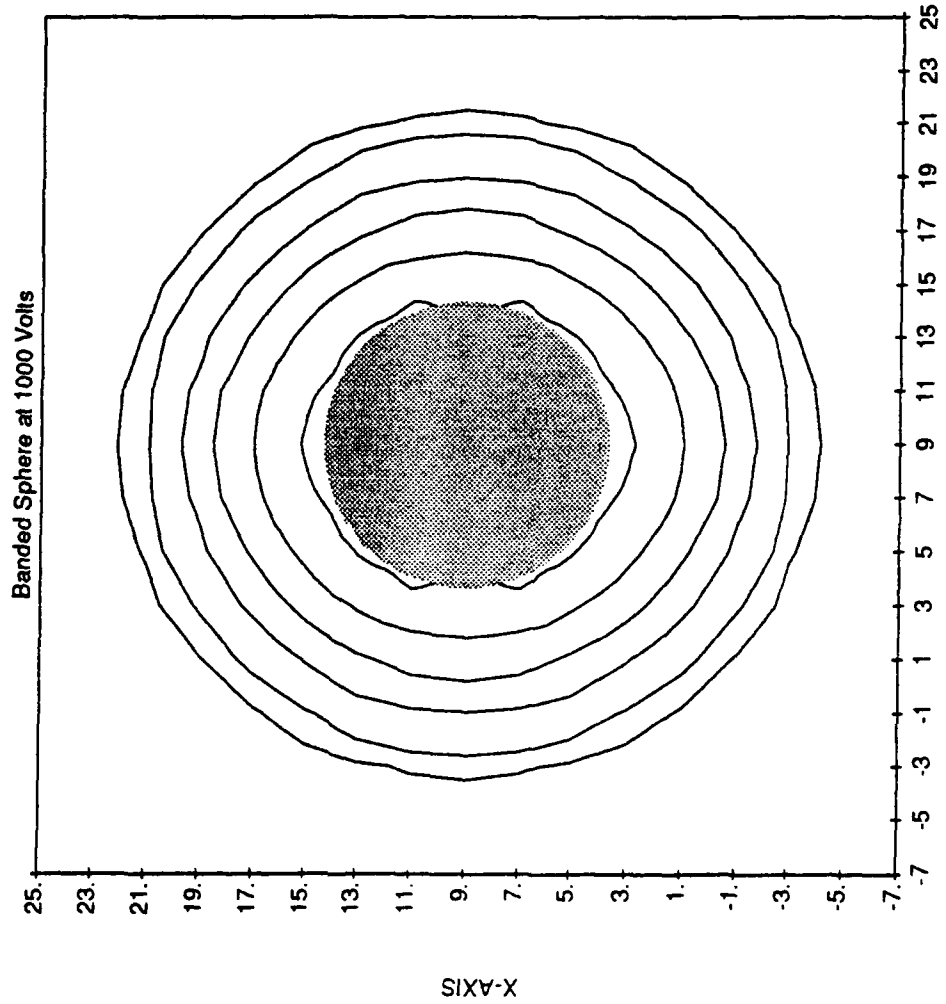


Minimum Potential = 0.00E+00 Maximum Potential = 1.00E+03
-7.00 <Y< 25.00, -7.00 <X< 25.00, CUTPLANE OFFSET Z= 9.00

5/15/92, 9:33:53

CNTR-LEVELS

- 1.00E+00
- 1.00E+01
- 2.00E+01
- 5.00E+01
- 1.00E+02
- 2.00E+02
- 5.00E+02
- 1.00E+03



Minimum Potential = 0.00E+00 Maximum Potential = 1.00E+03
-7.00 <Y< 25.00, -7.00 <X< 25.00, CUTPLANE OFFSET Z= 9.00

5/18/92 12:44:30

ATTACHMENT 1

Paper titled "Predicted Potentials and Currents for TSS-1," presented at the AIAA 30th Aerospace Sciences Meeting, Reno, Nevada, January 9, 1992.



The U.S. Government is authorized to reproduce and sell this report.
Permission for further reproduction by others must be obtained from
the copyright owner.

AIAA 92-0574
Predicted Potentials and Currents for TSS-1

V. A. Davis, I. Katz, and T. T. Luu
Maxwell Laboratories, Inc., S-Cubed Division
La Jolla, CA

M. R. Oberhardt
Geophysics Directorate, Phillips Laboratory
Hanscom Air Force Base, MA

30th Aerospace Sciences
Meeting & Exhibit
January 6-9, 1992 / Reno, NV

PREDICTED POTENTIALS AND CURRENTS FOR TSS-1

V. A. Davis, I. Katz, T. T. Luu

Maxwell Laboratories, Inc., S-Cubed Division, P. O. Box 1620, La Jolla, California 92038

M. R. Oberhardt

Geophysics Directorate, Phillips Laboratory, Hanscom Air Force Base, MA 01731

Abstract

The Tethered Satellite System 1 (TSS-1) is scheduled to fly on the space shuttle in mid-1992. The Shuttle Potential and Return Electron Experiment (SPREE) has been designed to monitor orbiter potential with respect to the ambient space plasma, measure return currents to the orbiter, and determine wave-particle interactions during the TSS-1 mission. The orbital motion induced $\mathbf{v} \times \mathbf{B}$ will generate substantial potentials across the 20 km conducting tether. This work reports our preflight calculations of the distribution of voltages among the tethered satellite system elements and the tether currents for the range of plasma conditions expected during the mission. Ion collection by the orbiter was calculated in three dimensions for several orientations, potentials, and plasma conditions using NASCAP/LEO. The calculated orbiter collection along with the core electron gun perveance were incorporated into EPSAT, which integrates models of spacecraft environment interactions, to perform a mission analysis. The analysis shows potentials over 2 kV are expected on the subsatellite surface when the ionospheric plasma density is low. The orbiter may charge as much as a kilovolt under these conditions. When the gun is not operating, the orbiter could charge over 1 kV, if care is not taken. Currents as high as 250 mA are expected for peak ambient density. The orbiter ion-collecting sheath impedance ranges from 10 to 100 k Ω . We also examined the possibility of current enhancement by the subsatellite neutral gas thrusters.

Introduction

The Tethered Satellite System 1 (TSS-1) is a space shuttle-based experiment that is scheduled to fly in mid-1992. The project involves several American and Italian research groups. A meter-radius, spherical subsatellite will be reeled out upward from the orbiter on the end of a 20 km conducting tether. The induced $\mathbf{v} \times \mathbf{B}$ along the tether wire can be 5 kV. The current flow through the tether will be limited by the ability of the orbiter to collect current (collect ions and emit electrons) and the subsatellite to emit current (collect electrons). Four electron guns will be on the orbiter

to emit electrons at times during the experiment. Two electron guns (core guns) are tied directly to the tether current, and an additional two electron guns are driven by an independent power supply.

Phillips Laboratory is providing the Shuttle Potential and Return Electron Experiment (SPREE). SPREE will measure the ion and electron distribution functions in the energy range from 10 eV to 10 keV, for fluxes ranging from 10^7 to 10^{16} $\text{m}^{-2}\text{s}^{-1}$.

Three-Dimensional Calculations of Orbiter Ion Collection

We examined orbiter ion collection as a function of orientation, potential, and plasma conditions using the three-dimensional analysis code NASCAP/LEO.^{1,2} NASCAP/LEO examines the interactions between high-potential spacecraft and the plasma environment in low-Earth orbit, including geometric and orientational effects.

The surface of the orbiter is primarily insulating, heat-resistant tiles. The insulating surfaces remain at the plasma potential in the high-density, low-temperature plasma of low-Earth orbit. Ion collection by the orbiter engine bells is the only significant current source, other than the electron guns. The orbiter model used in the calculations is shown in Fig. 1.

We examined ion collection as a function of orientation. Fig. 2 shows the orientation and the rotation axis. Fig. 3 shows the variation in current collected with angle. For these calculations, an ambient plasma of 10^{12} m^{-3} and 0.1 eV was used. An orbiter potential of -300 V and a ram velocity of 7500 ms^{-1} is used. At 0° , the orbiter is traveling with its belly facing the ram directly and the engine nozzles in the wake; thus, little current is collected. As the orbiter rotates, more of the engine nozzles are exposed to the ram side of the orbiter and more current is collected. At 90° , the orbiter is moving sideways to the ram, and the sides of the nozzles are exposed to the ram. The current to the nozzles' sides peaks at this point and remains steady. At 180° , the nozzles face the ram direction, and the current to the faces of the engine nozzles peaks. Unless the engine bells are in the ram, little ion current is collected.

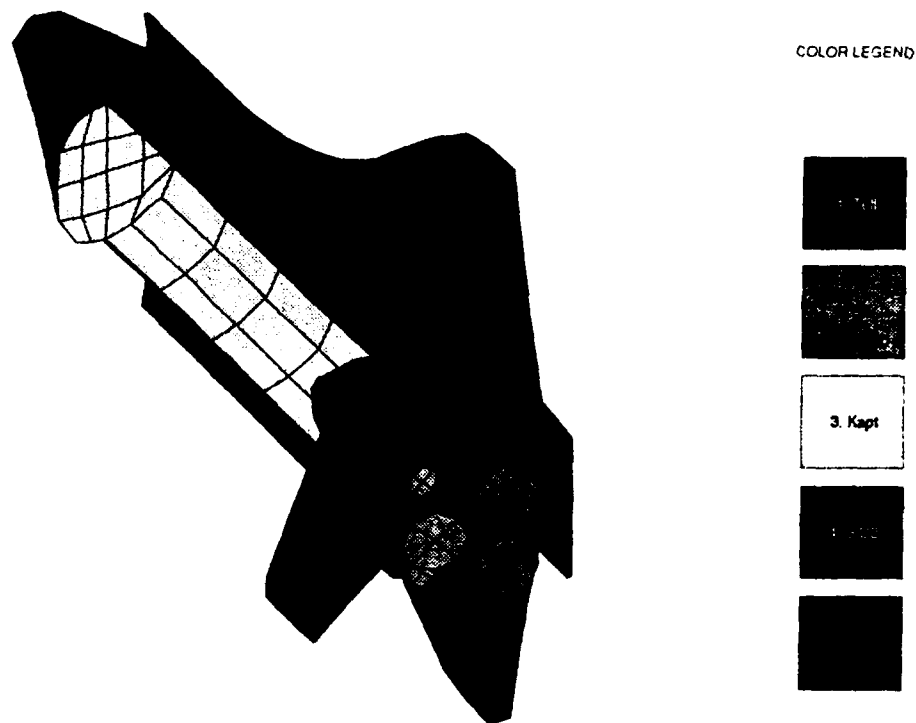


Fig. 1. Patran model of orbiter used for NASCAP/LEO calculations of ion collection.

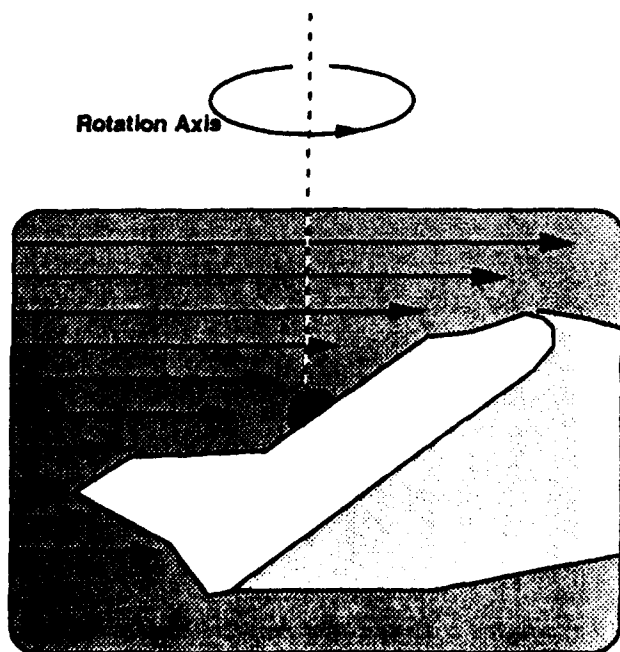


Fig. 2. Orbiter orientations used in these calculations.

We also examined ion collection as a function of potential and plasma density. The results are in Fig. 4. The bay-to-ram orientation is 180° and the belly-to-ram orientation is 0° . At the higher potentials, the orbiter orientation is less critical. This is because as the sheath grows larger, the fraction of the sheath edge obstructed by the rest of the orbiter (other than the engine bells) shrinks.

High potentials are needed in order for the orbiter to collect substantial currents. Fig. 5 shows the effective impedance for the same cases shown in fig. 4. The effective impedance is near $100 \text{ k}\Omega$ at low density.

Mission Analysis

A mission analysis without geometry effects has been completed using the EPSAT computer code.³ The subsatellite and orbiter potentials and the tether current vary as the plasma density changes over the orbit. EPSAT is designed specifically to perform this type of study. The code contains a system definition module, an orbit definition module, natural environment modules, system-generated environment modules, and analysis modules. Each module has access to the results of calculations performed by the other modules. The modules used in these calculations

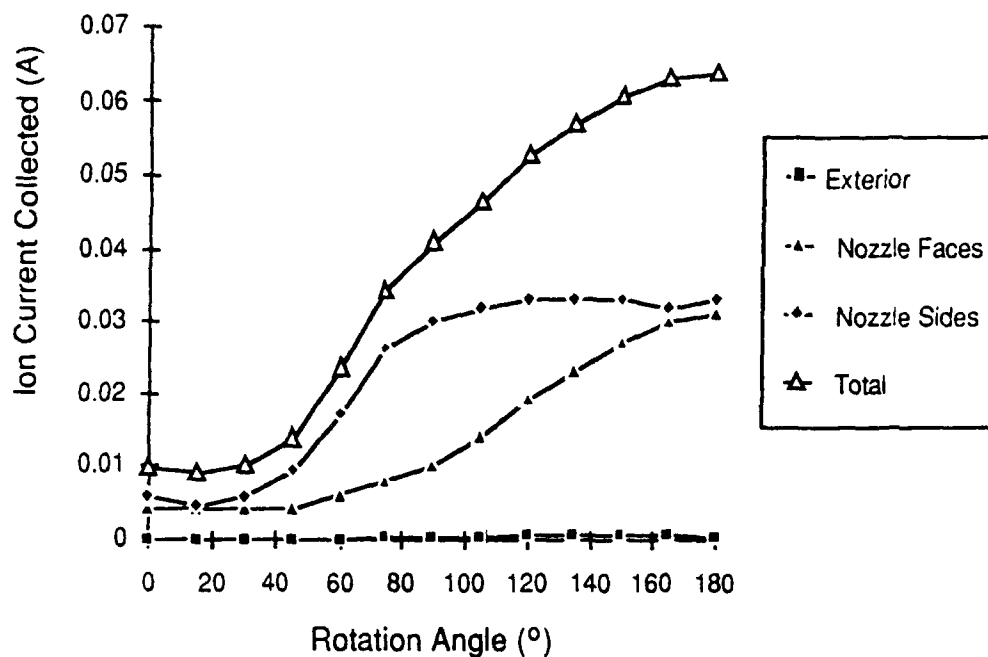


Fig. 3. Ion currents versus rotation angles.

include the ORB orbit generator, MSIS-86 neutral densities, IRI-86 plasma densities, as well as S-Cubed-developed system definition, floating potential, and nozzle modules. The floating potential model includes models for particle collection by sheaths and emission by electron guns.

The subsatellite collects electrons from the ambient plasma through a sheath. The orbiter engine bells collect ions from the ambient plasma through a sheath. The electron guns emit electrons. The floating potential is the potential at which no net charge is accumulated. The current collected by the subsatellite at this potential is the tether current.

Fig. 6 shows the variation in subsatellite floating potential and tether current over a few orbits. The core gun with a perveance of 3.8×10^{-6} is operating during the entire period. The net resistance of the subsatellite paint, tether wire, and shunt is taken to be $10 \text{ M}\Omega$. (A shunt is placed in the circuit to control the tether current.) The tether current varies from 75 mA to 250 mA. Over the same period the subsatellite potential varies from 150 V to 2.3 kV.

Bulk Ionization at the Subsattellite

We also used EPSAT to examine the neutral densities and the likelihood of breakdown at the subsatellite due to outgassing, leaking thrusters, or thruster firings. In order to

determine if enough neutral atoms will be outgassed from the subsatellite to present a risk of bulk ionization, we examined outgassing densities for the case where all the surfaces emit 0.5 W m^{-2} . This is the outgassing rate of G-10 after exposure to air and provides an upper bound. Fig. 7 shows the neutral densities about the subsatellite due to outgassing at this rate. The column density of outgassed neutrals from a point just outside the subsatellite to a point 2.88 m away (the Parker-Murphy radius for a 3.6 kV sphere) is $1.6 \times 10^{17} \text{ m}^{-2}$. With a cross section of $3 \times 10^{-20} \text{ m}^{-2}$, the ionization fraction (number of ionizations as a fraction of the number needed to cause ionization) is 0.0048. EPSAT estimates the ionization fraction to be 0.15 when the space-charge sheath size is used as the average path length. Breakdown is expected when the ionization fraction approaches 1. Since the the outgassing rate used in these calculations is orders of magnitude higher than expected and the sheath size is the largest expected, no bulk ionization is expected from outgassing alone.

The EPSAT nozzle model was used to model one nozzle of one of the 2 N in-line thrusters on the subsatellite. Figs. 8 show the gas density about the subsatellite with operation of one nozzle. The column density for a 2.88 m (the Parker-Murphy radius) column offset from the axis of the nozzle by 0.51 m is $5 \times 10^{20} \text{ m}^{-2}$. This gives an ionization fraction greater than unity, implying sheath ionization is to be expected during operation of even one thruster.

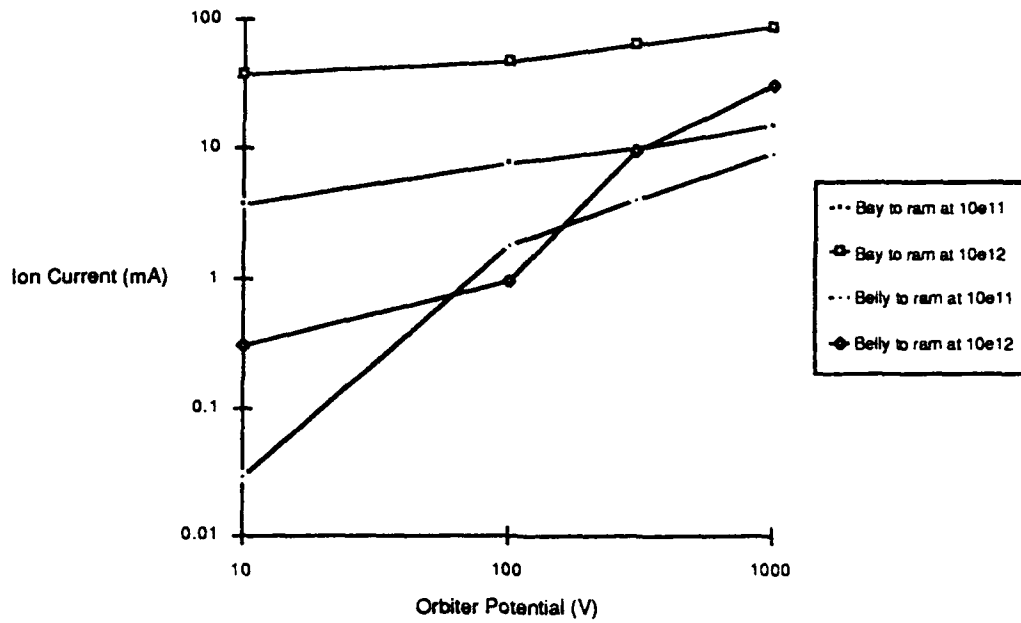


Fig. 4. Ion currents versus potential for various conditions.

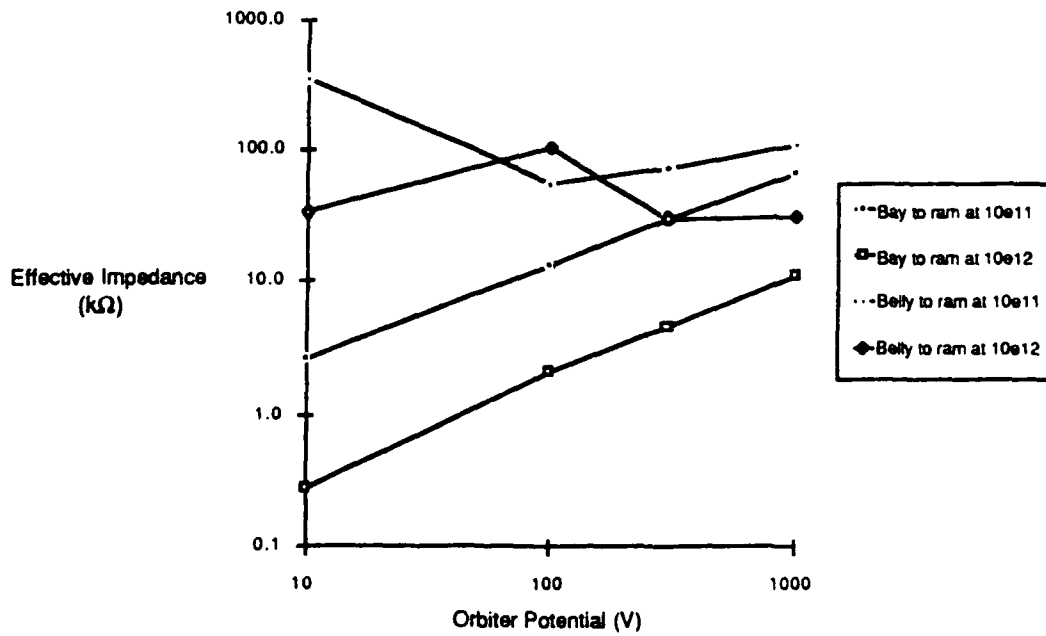


Fig. 5. Effective impedance versus potential for various conditions.

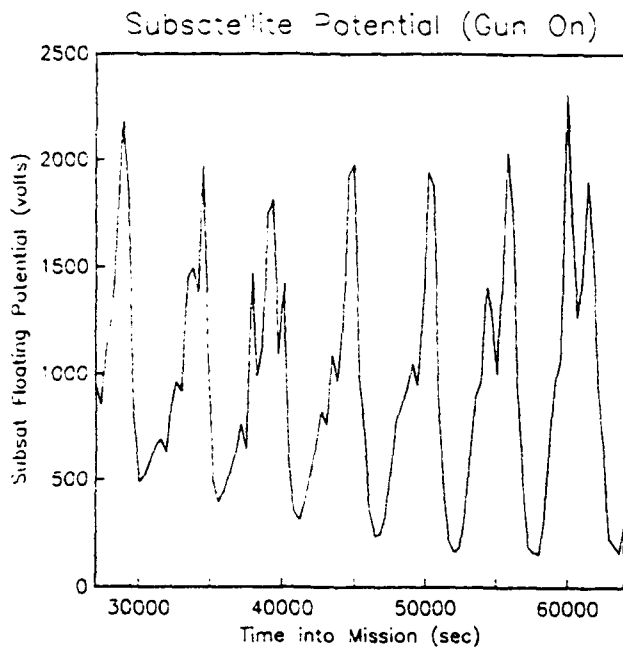


Fig. 6a. Variation in subsatellite potential over a few orbits.

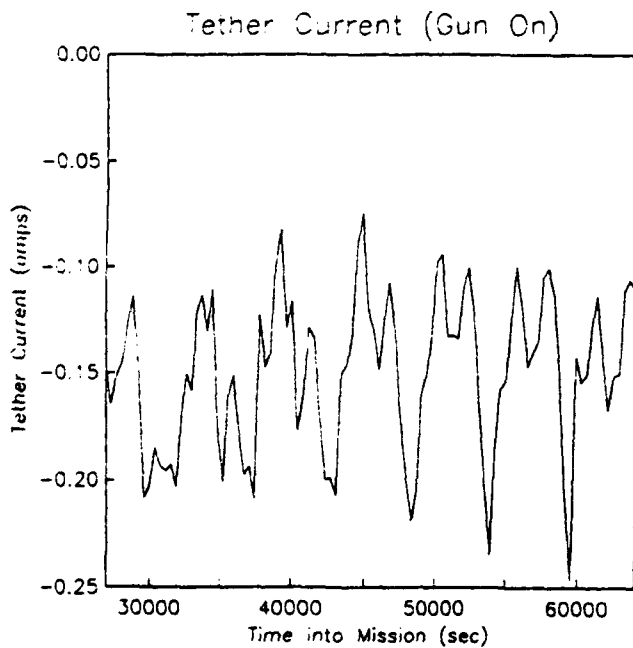


Fig. 6b. Variation in tether current over a few orbits.

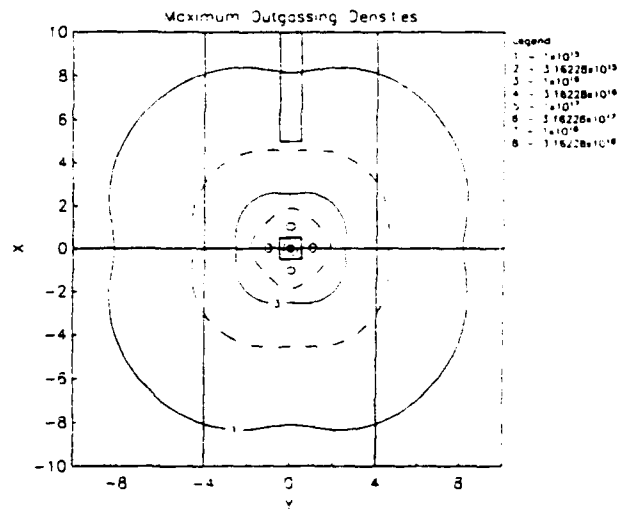


Fig. 7. Neutral densities about the subsatellite from outgassing at 0.5 W m^{-2} , which is a maximal rate. The units of position are meters and of density are molecules per cubic meter.

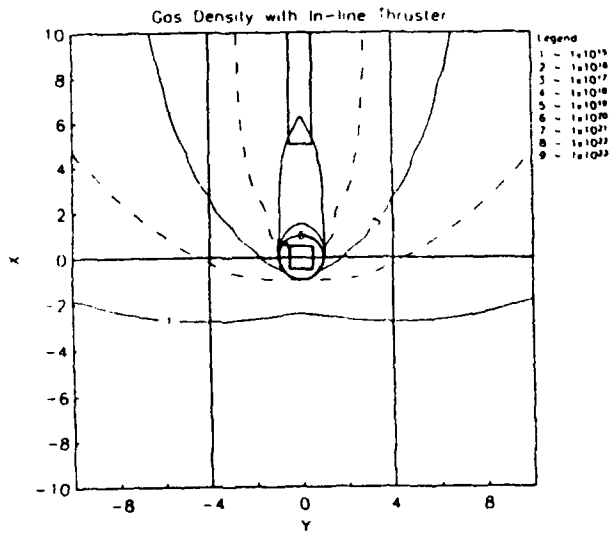
Summary

The small conducting area of the orbiter limits the ion current that can be collected. The effective impedance can be as high as $100 \text{ k}\Omega$ at low plasma densities. The orientation of the orbiter can affect the current collected by a factor of 7.

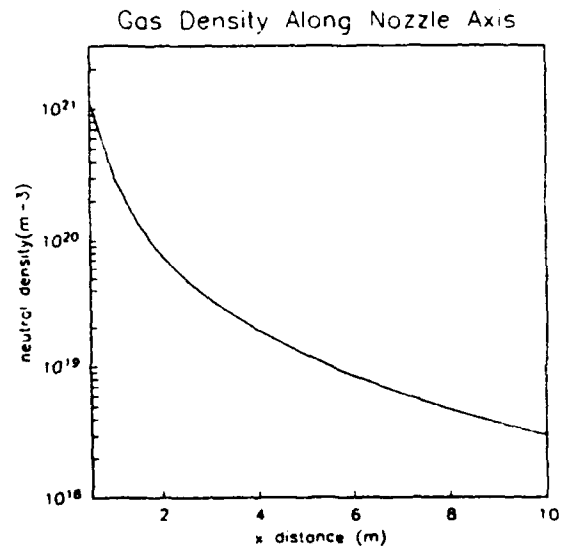
During operation of the core gun, the tether current will vary from 75 mA to 250 mA as the orbiter moves through regions of high and low plasma density. The subsatellite potential will vary from 150 V to 2.3 kV , and the orbiter potential will vary from -400 V to -1.1 kV .

Using upper bounds on the outgassing rate, outgassing does not provide enough gas density for sheath ionization to occur. However, the firing of even one thruster generates enough gas for sheath ionization.

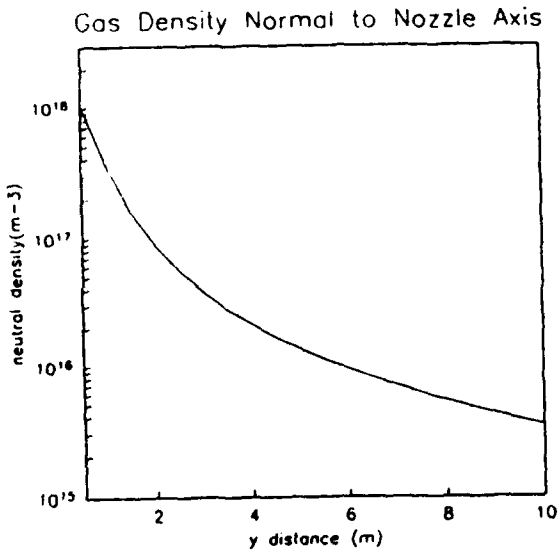
During thruster firings, the current collected by the subsatellite will dramatically rise. The tether current will be limited by the electron gun perveance and the tether impedance. In addition, caution will need to be exercised to ensure that the sheath ionization will not damage the subsatellite equipment.



(a)



(b)



(c)

Fig. 8. Gas densities due to one nozzle of the 2 N in-line thruster. (a) is a contour plot. (b) and (c) show the gas density along the thruster axis and normal to the nozzle axis. All distances are in meters and all gas densities are in molecules per cubic meter.

Acknowledgements

This work was funded by the U. S. Air Force Phillips Laboratory, Geophysics Directorate, Hanscom Air Force Base, Massachusetts.

References

¹ Mandell, M. J. and Davis, V. A., "User's Guide to NASCAP/LEO," S-Cubed Report SSS-R-85-7300-R2, August, 1990.

² Mandell, M. J. and Katz, I., "High-Voltage Plasma Interactions Calculations Using NASCAP/LEO," AIAA Paper No. 90-0725, January, 1990.

³ Jongeward, G. A., Kuharski, R. A., Kennedy, E. M., Wilcox, K. G., Stevens, N. J., Putnam, R. M., and Roche, J. C., "The Environment-Power System Analysis Tool Development Program," in Proceedings of the 24th Intersociety Energy Conversion Engineering Conference, Washington, DC, August 6-11, 1989.